REVISION 1

Hydrothermal mineral replacement reactions for an apatite-monazite assemblage in alkali-rich fluids at 300 – 600 °C and 100 MPa

Wladyslaw B. Betkowski[1], Daniel E. Harlov[2,3], and John F. Rakovan[1]

[1]Miami University, Department of Geology and Environmental Earth Science, 114 Shideler Hall, Oxford, OH 45056 (betkowwb@miamioh.edu)

[2]GeoForschungsZentrum Potsdam, Telegrafenberg, D-14473 Potsdam, Germany

[3]Department of Geology, University of Johannesburg P.O. Box 524, Auckland Park, 2006 South Africa

Abstract

Mineral replacement reactions are common in the various environments where rocks have undergone re-equilibration with geologic fluids. Replacement reactions commonly take the form of fluid-aided, coupled dissolution-precipitation and often result in pseudomorph formation. One class of environment that frequently shows significant examples of mineral replacements is hydrothermal ore deposit systems. The goal of this study was to test the simultaneous reactivity of fluorapatite and monazite in Na and Si-rich hydrothermal fluids,

which partially mimic the mineralogy and fluid chemistry of the Llallagua tin deposit in Bolivia. A series of experiments were performed at 300 to 600 °C and 100 MPa, utilizing various combinations of monazite, fluorapatite, and H_2O + $Na_2Si_2O_5$. Reaction products were evaluated using scanning electron microscopy, electron microprobe analysis, and single crystal x-ray diffraction. The results of this experimental study show that fluorapatite and monazite are differentially reactive under the conditions studied. The reaction products, pathways, and kinetics have a large temperature dependence. The 300 and 400 °C experiments show variable amounts of monazite replacement and only minor, if any, dissolution or reactivity of fluorapatite. The high-temperature 500 and 600 °C experiments are characterized by massive replacement of monazite by vitusite and britholite. Exclusively at 600 °C, monazite alteration takes the form of symplectite development at the reaction front as vermicular intergrowths of vitusite and britholite. The higher temperature experiments also show substantially more reactivity by fluorapatite, which is partially pseudomorphically altered into britholite. This is an example of regenerative mineral replacement where both fluorapatite and britholite share the same atomic structure and are crystallographically coherent after the partial replacement. The britholite replacement is characterized by the presence of oriented nanochannels, which facilitate fluid-based mass transfer between the bulk solution and the reaction front. The fluorapatite replacement is enhanced by monazite alteration through a self-perpetuating, positive feedback mechanism between these two reactions, which enhance the REE mobility in alkali-bearing fluids and further drives bulk re-equilibration. These results have potential geochronologic implications and may be significant in the evaluation of monazite and

fluorapatite as potential solid nuclear waste forms. They also give us deeper insights into the mechanism of mineral replacement reactions and porosity development.

Keywords

selective mineral replacement, dissolution-precipitation, fluorapatite, monazite, britholite, pseudomorphism, multi-phase reaction

Introduction

Multi-phase, fluid-mineral interactions are ubiquitous in hydrothermal environments and in the precipitation of primary and secondary ore and accessory minerals. From these interactions, an important class of reactions is re-equilibration reactions involving the dissolution of unstable minerals and the precipitation of stable minerals. Numerous studies have demonstrated that such reactions can be both spatially and temporarily connected taking the form of a dissolution-reprecipitation process, which includes site-specific ion exchange within the same mineral or mineral family members. This leads to a change in the relative amounts of major or trace elements analogues to a substitution process within a solid solution series. Apatite [$Ca_5(PO_4)_3(F,Cl,OH)$] and monazite ($LREEPO_4$) are well known as geochemical tracers from their broad range of compositions as a function of P-T-X conditions (Bhowmik et al. 2014; Harlov 2015). They are also primary repositories for REE, Y, U, and Th (Pan and Fleet 2002; Hughes and Rakovan 2015), and their reactivity in a variety of fluids can control the abundance and mobility of these elements in hydrothermal systems and melts (e.g. Rapp and Watson 1986). Due to their common accessory character and high closure temperature, monazite and fluorapatite can

be successfully used as analogous geochronometers (Torab and Lehmann 2007; Williams et al. 2011; Kusiak et al. 2014; Chew and Spikings 2015). Previous studies have shown enhanced monazite reactivity and replacement textures in alkali rich fluids and brines (Budzyń et al. 2011; Harlov and Wirth 2012). In contrast, fluorapatite is much more reactive in acidic solutions (Harlov and Förster 2003; Harlov et al. 2005), which suggest the potential for differential reactivity if both fluorapatite and monazite are present in a system.

One example, where alkali rich fluids could be responsible for selective hydrothermal alteration of primary fluorapatite and monazite, is the Llallagua tin deposit, Bolivia(Rakovan et al. 1997; Kempe et al. 2008; Kohn and Vervoort 2008). Throughout the first half of the 20th century the Llallagua deposit was one of the World's largest Sn producers with a historical production of about 500,000 metric tons. The hydrothermally altered porphyry of the Salvadora stock in Llallagua is part of the Bolivian Tin Belt situated in the Andes Mountains. Based on SiO_2-Zr/TiO_2 discrimination plots, the stock was likely of a dacitic to rhyodacitic composition (Dietrich et al. 1997), but is pervasively metasomatized to sericite, tourmaline, and quartz. The Sn mineralization (cassiterite - SnO_2) is hydrothermal in origin and is believed to be closely genetically and temporally related to the emplacement of the Salvadora volcanic stock (Sillitoe et al. 1975). Unlike most deposits in the Bolivian Tin Belt, phosphate minerals are common at Llallagua. Fluorapatite is one of earliest formed minerals in the hydrothermal veins overlapping and subsequent to quartz. Monazite is also thought to have formed early in the vein paragenesis and is closely intergrown with quartz and cassiterite. Recent studies have revealed geochronologic inconsistencies between fluorapatite and monazite, which is speculated to be the result of selective mineral replacement (Rakovan 2013; Betkowski et al. 2015).

In order to test hypotheses for the selective replacement of monazite and fluorapatite in Llallagua, a series of hydrothermal experiments utilizing natural fluorapatite and monazite from Llallagua, or their synthetic analogues, were performed employing Na and Si-rich fluids (H_2O + $Na_2Si_2O_5$). The experiments consist of 12 separate runs at temperatures ranging from 300 to 600 °C at 100 MPa. The temperature limits for the experiments were chosen based on fluid inclusion studies of quartz from Llallagua (Grant et al. 1980; Sugaki et al. 1988). These studies indicated homogenization temperatures between 441°C and 262°C and salinities from over 21 NaCl equivalent down to 4.7 NaCl eq. The pressure used in the experiments was selected based on the shallow subvolcanic association of the Llallagua deposit, which was also documented for similar deposits within the Bolivian Tin Belt with pressures ranging from around 15 MPa to 200 MPa (Kelly and Turneaure 1970; Kontak and Clark 2002). The fluid used in these experiments was chosen to broadly simulate chemistries, enriched in Na and Si, that were involved in the hydrothermal alteration of Llallagua porphyry. This is deduced based on mineral associations found within the vein paragenetic sequence which includes quartz, as the most abundant gangue mineral, but also locally ubiquitous Na-bearing tourmalines, which were formed during the main stage of metasomatic alteration (Sillitoe et al. 1975). Furthermore, fluid inclusions studies suggest Na as a major fluid component and fluid inclusions occasionally contain Na-bearing dawsonite daughter crystals (Sugaki et al. 1988). Among these experiments, those at 300 and 400 °C are particularly intended to simulate the P-T conditions extant during formation of the hydrothermal mineralization at Llallagua. The 500 and 600 °C experiments were performed to study the enhanced kinetics of dissolution and reprecipitation and mobility of REEs. Although Llallagua was the initial impetus for this study,

the common presence of high Na and Si activities in hydrothermal fluids makes these experiments relevant to other systems where both apatite and monazite are present; including engineered systems such as mixed phase solid nuclear waste forms.

Experimental and analytical methods

The natural fluorapatite and monazite, taken from the Llallagua vein samples, consists of subhedral to euhedral, relatively transparent and inclusion-free grains. They were hand picked out of rock samples and crushed to 100 to 250 µm sized fragments in ethanol. Any foreign minerals, as well as cloudy grains, were separated out by hand picking and the remaining grains were washed in ethanol in an ultrasonic bath. Additionally, monazite and fluorapatite crystallinity were analyzed using single crystal x-ray diffraction and their well crystalline, non-metamict nature was confirmed by the presence of sharp, isolated diffraction spots. Under high contrast back scattered electron (BSE) imaging, polished cross sections of the monazite and fluorapatite grains indicate some hydrothermal zoning controlled by the behavior of REEs (Fig. 1b). Fabrication of the pure synthetic fluorapatite and LREE monazite used in this study are given in Schettler et al. (2011) and Tropper et al. (2013), respectively.

Each experimental charge consisted of 15 or 20 mg of fluorapatite +/- 5 mg monazite plus 10 mg of $Na_2Si_2O_5$ plus 10 mg H_2O (Tab. 1). The experimental charge was placed in a 3 mm wide, 1 cm long Au capsule, which was arc-welded shut. Experiments were conducted at 300, 400, 500, and 600 °C at 100 MPa (Tab.1). The length of the experiments was planned based on the temperature. The 300 °C experiments were left up for 50 days, compared with 600 °C, which

were left up for 13 days. The experiments were carried out using standard cold seal autoclaves in conjunction with a hydrothermal high-pressure line. The internal thermocouple was placed such that the tip was half way up along the Au capsules at the end of the autoclave. Thermocouples are accurate to within ± 3 °C. No variation in temperature was observed during any of the runs. The maximum temperature gradient along the length of a capsule was approximately 5 °C. Pressure on the hydrothermal line was calibrated against a pressure transducer calibrated against a Heise gauge manometer for which the quoted pressure is accurate to ± 5 MPa. After the run, the autoclave was quenched using compressed air. Temperatures of 100 °C were generally reached within 30 to 60 seconds.

After each experiment, the autoclave was opened and the four Au capsules extracted. Each Au capsule was cleaned, weighed (to check for fluid loss during the experiment), and then punctured. The Au capsules were then dried at 105 °C for several hours, and weighed again to determine fluid loss. Trace element analysis of the fluid was not done. The charge was mounted in an epoxy grain mount and then polished.

All extracted material was evaluated by a combination of field emission (FEG) scanning electron microscopy (SEM), chemical analysis and X-ray diffraction. Experimental charges were first studied using high-contrast back scattered electron (BSE) imaging on a Zeiss Supra 35 VP FEG-SEM at the CAMI Center for Advanced Microscopy, Miami University, with an accelerating voltage 20 KeV and 4.5-5.5 mm working distance. The subsequent energy dispersive spectroscopy (EDS) measurements were performed using an EDAX Genesis 2000 XEDS. Electron microprobe (EMP) analyses were made on a JEOL JXA-8500F HYPERPROBE at the Deutsches GeoForschungsZentrum, Potsdam, equipped with a thermal field emission gun. Operating

conditions included a 20 kV, 40 nA, 2 µm diameter electron beam for monazite, vitusite [$Na_3(Ce,La,Nd)(PO_4)_2$], and sazhinite [$Na_2Ce[Si_6O_{14}(OH)] \bullet n(H_2O)$] and a 20 kV, 20 nA, 2-15 µm electron beam spot for fluorapatite and britholite [$(REE,Ca,Na)_{10}(SiO_4,PO_4)_6(OH,F)_2$]. Primary standards included pure metals for Th and U, vanadinite for Pb, synthetic REE phosphates prepared by Jarosewich and Boatner (1991), synthetic oxides, and natural minerals such as the Durango fluorapatite. Analytical errors for the REE in monazite depend on the absolute abundances of each element. Relative errors are estimated to be < 1% at the > 10 wt% level, 5−10% at the 1 wt% level, 10−20% at the 0.2 to 1 wt% level, and 20−40% at the < 0.1 wt% level. For concentrations below 0.1 wt%, the analytical precision for the actinides and lead is much higher, i.e., approximately 10%. Detection limits were approximately 500 − 1000 ppm for the REE, 200 – 300 ppm for Th and U, and 100 ppm for Pb. EMP measurement of Cl and F in fluorapatite were made according to guidelines outlined in Stormer et al. (1993).

Several EMP line scans were made across reaction boundaries and the overgrowths on the fluorapatite. In these Si, Ce, Na, Ca, and P were analyzed (x-ray counts number) using a 3.015e-09A, 20 kV focused beam. Each spot was measured for 1000ms and was integrated over 5 accumulations using movable WDS spectrometers. The WDS mapping was performed under 4.9-5.0 nA and 20 kV focused beam conditions. Depending on scale, the maps resolutions vary between 0.1 and 0.2 µm per pixel. In addition to chemical analysis, X-ray powder diffraction identification of experimental products was done using a Scintag X1 Powder Diffractometer combined with the phase search routine using MDI Jade 9 software.

Experimental Results

300 °C experiments

At 300 °C, the sole fluorapatite-$Na_2Si_2O_5$ experiment (LAM5, Tab.1) shows no fluorapatite reactivity, i.e. a minority of the fluorapatite grains has very minor serrations along certain surfaces (Fig. 2a). In the monazite experiments, the crystal fragments are partially corroded and partially replaced by vitusite and to a lesser extent by sazhinite (Fig. 3).

The formation of vitusite normally occurs in close proximity to the monazite as required by the high concentration of $(PO_4)^{3-}$ and REE necessary for its formation. Much less commonly, vitusite can be found growing directly as elongated pseudohexagonal crystals in the $Na_2Si_2O_5$ + H_2O matrix (Fig. 3). In both the synthetic and natural experiments at 300 °C, the subhedral monazites are predominantly embedded in euhedral sazhinite, which is volumetrically the dominant mineral phase after the reaction.

The co-existence of vitusite and sazhinite in the same experiment results in a redistribution of the LREEs and HREEs compared to monazite (R=∑HREE/∑REE x 100%). In the Llallagua monazite (the number of microprobe analysis (n)= 15;) R is 5.9%, while for vitusite (n = 6) R is 2.1%, and for sazhinite (n = 7) R is 11.4%. This shows that volumetrically dominant sazhinite also has a higher affinity for HREE than the less abundant vitusite. Although overall, vitusite is the more REE-rich phase with an avg. REE_2O_3 equal to 39.27 wt% vs. 25.18 wt% for sazhinite.

400 °C experiments

At 300 °C the estimated ratio of sazhinite to vitusite in the reaction products is 5:1. But with a temperature increase to 400 °C, the volume proportions become roughly equal. Temperature increase favors the formation of $(PO_4)^{3-}$ and REE-rich vitusite as a ubiquitous phase in both the natural and synthetic phosphate experiments. At the same time, the temperature increase has only a limited effect on the reactivity of fluorapatite, which starts to exhibit the first signs of very weak dissolution (Fig. 2b). Sazhinite often mantles the monazite, which has been partially pseudomorphically replaced by vitusite as shown in Fig. 4.

In the 400 °C experiments, minute crystals of britholite are observed for the first time. They are seen both in the experiments utilizing natural and synthetic phosphates. Britholite forms a 1 to 2 µm thick partial corona structure. They comprise 0.5 to 1 µm subhedral, subparallel crystals elongated perpendicular to the fluorapatite grain surface. The perpendicular elongation of the britholite crystals with respect to the fluorapatite suggests an epitaxial relationship between the fluorapatite and britholite. The britholite is characterized by low REE totals but a high P and Ca content with a significant vacancy on the Ca site. This is due to two coupled substitution reactions (cf. Pan and Fleet, 2002):

$$2REE^{3+} + \square \leftrightarrow 3Ca^{2+} \quad (1)$$

$$REE^{3+} + Si^{4+} \leftrightarrow Ca^{2+} + P^{5+} \quad (2)$$

500 °C experiments

A temperature increase from 400 to 500 °C has a major influence on the behavior of fluorapatite and monazite. At 500 °C, the reaction products include vitusite forming thick replacement rims around monazite and britholite, which mainly overgrows and replaces the fluorapatite. Sazhinite is no longer present. The higher temperature is reflected in the higher degree of reactivity despite the shorter duration of the experiments (37 days).

In the monazite-absent experiments, the Llallagua fluorapatite reacted only with $Na_2Si_2O_5$ and shows a substantial etching texture with the formation of long dissolution channels parallel to the *c*-crystallographic axis (Fig. 2c). This apparent increase in the length of dissolution channels, paired with a decrease in the experimental duration, suggests a substantially higher reactivity for fluorapatite at this temperature. Here, some of the fluorapatite crystals show patches of diminished BSE intensity identified as zones depleted in F. Because there is no Cl in the system, OH is presumed to be the substituting anion. Under high contrast BSE imaging, a sharp reaction front is seen between the altered and unaltered zones.

In experiments with fluorapatite and monazite, vitusite is the dominant phase forming an overgrowth-replacement texture around monazite, and is also found as euhedral, pseudohexagonal crystals within the reaction product fabric. Figure 5a shows a replacement texture associated with the synthetic monazite. Isolated remnants of a single monazite are embedded in the vitusite. The vitusite zone is heavily cracked but otherwise featureless. The vitusite zone is encompassed by and intergrown with BSE-bright, minute crystals of britholite. The morphology of the external britholite corona (Fig. 5a-[2]) follows the shape of the vitusite zone. All but one of the borders of the britholite corona lie in the proximity of vitusite and reflect the major features of its concave and convex shape. This implies that the britholite

crystals were nucleated either in direct contact with the vitusite or with the original monazite before its partial replacement by vitusite. Figure 5b shows a natural monazite that is partially replaced and surrounded by a britholite corona, which has formed within the vitusite zone. The corona follows the exact shape of the monazite crystal, suggesting that the britholite nucleated in close proximity to the monazite grain at the beginning of the dissolution process. This would imply that the vitusite (Fig. 5b-[1]) formed as a replacement product at the expense of the dissolving monazite. Despite the same experimental duration, the monazite replacement textures are characterized throughout by various stages of completeness. The monazite shown in Fig. 6 is partially replaced by vitusite which itself is surrounded by a fined grained britholite corona. The replacement is overgrown by well-defined vitusite crystals. On the right side of the image, there is a zone of highly porous vitusite, which is interpreted as the very last stage of growth, after the complete dissolution and replacement of monazite.

Britholite, which is a major phase at 500 °C, can form both as an overgrowth and as a replacement of fluorapatite and is a major sink for REE. One case where britholite creates an overgrowth is shown in Fig. 7. Overgrowth is suggested by the morphology of the fluorapatite with well-preserved sharp edged crystal faces, but also from the faceted habit of the britholite itself. The overall shape of the fluorapatite does not exhibit significant modifications from the initial morphology of the other fragmented grains used in the experiment. The overgrowth is free of significant pore space and, as such, it is not permeable to the bulk hydrothermal fluids. The britholite overgrowth shields the fluorapatite from fluids preventing dissolution and modification of its initial shape. Britholite overgrowths are commonly characterized by chemical zoning (Fig. 8a). The composition of the britholite overgrowth near the fluorapatite grain

surface is REE-rich, which produces a bright BSE signal. Far from the fluorapatite, more Ca and P are incorporated within the britholite, with a corresponding drop in Si and REE (Fig. 8c). The gradual enrichment in Ca and P is visible throughout the entire profile but especially after the crossing of the concentric zone labeled #2 (Fig. 8a-[2]). This transition corresponds to the beginning of a dark, outer zone (Fig. 8b). The more detailed pattern is presented in Figure 8d demonstrating a boundary between a BSE-light/dark zone over a short scan distance (line length = 18µm). EMP data confirm a REE decrease over the scan length (from the light zone into the dark) from 5.43 to 4.86 REE apfu. Additionally, the REE concentrations in the #1 and #2 zones exceed the neighboring zones by at least 1 wt% REE_2O_3 (LAM3-1/V-IX at Tab. 2). The transition from a BSE bright to a BSE dark region corresponds with a change in the REE fraction incorporated via coupled substitution reactions (2) and (3) (cf. Pan and Fleet, 2002):

$$Na^{+} + REE^{3+} \leftrightarrow 2Ca^{2+} \qquad (3)$$

Coupled substitution reaction (2) decreases from 54.8% to 50.0%, whereas coupled substitution reaction (3) increases from 45.2% to 50.0%. The disproportion between Ca and P also increases across the overgrowth from the contact with the fluorapatite to the rim with a rise in Ca of 37% vs. 18.2% for P.

In addition to pure overgrowths, britholite can also constitute mixed overgrowth-replacement textures. In Fig. 9a, the fluorapatite is overgrown by a single ~20 µm thick uniform layer of britholite (Fig. 9a-[1]). Another distinctive feature is a zone of dissolved porous fluorapatite, which is incompletely filled by small elongate britholite grains (Fig. 9a-[2]). The texture suggests that the britholite is polycrystalline; however an epitaxial relationship with the

fluorapatite is likely. The britholite, which was nucleated as a replacement in a dissolution cavity after apatite, is significantly different from britholite overgrowing the fluorapatite. Element maps in Fig. 9b-e show a sharp chemical boundary between the two types of britholite and suggest both a replacement and overgrowth process. During dissolution of the fluorapatite, the reaction front is enriched in Ca, P, and F, which have to be removed into the bulk in order to support fluid undersaturation at the reaction front, which is necessary for the reaction to proceed (Putnis 2009). Initially, within the porous zone, both P and Ca show a steep decrease from the surface of the fluorapatite grain outwards, which is related to dissolution and transport processes. However, after crossing the overgrowth boundary P and Ca increase with increasing distance from the fluorapatite (Fig. 9b). REE (here represented by Ce) are present from the fluorapatite dissolution front up to the overgrowth boundary and across the overgrowth (Fig. 9c), which suggests their mobility in the fluids at the reaction front. Tight britholite development in the fluorapatite replacement zone is present in Fig. 10. The amount of space gained from fluorapatite dissolution and the space filled by newly formed britholite is similar (Fig. 10a,b-[1]). The small negative volume difference between the parent fluorapatite and the product britholite is visible through the development of an oriented porosity in the britholite. The porosity takes the form of evenly distributed nanochannels (or grain boundaries), which are oriented parallel to the britholite and fluorapatite *c*-axis direction. The replacement zone is in contact with the massive britholite overgrowth (Fig. 10a,b-[2]).

600 °C Experiments

Experiments at 600 °C produced the highest volume of altered and dissolved fluorapatite and monazite. In experiments with synthetic fluorapatite and $Na_2Si_2O_5 + H_2O$, the fluorapatite developed uniform dissolution features, such as a 150 µm long dissolution channel cross-cutting the entire fluorapatite crystal (Fig. 2d). When compared with the experiments conducted at 500 °C, the length of the dissolution pits is greater despite the shorter duration of the experiments (Tab.1).

In experiments with monazite and fluorapatite, monazite exhibits extensive vitusite replacement and overgrowth. Additionally, monazite alteration is commonly accompanied by the formation of vermicular britholite grains in the form of a symplectite intergrowth. Figure 11 shows the development of a symplectite texture around a monazite grain. The symplectite texture originates at the monazite reaction front and consists of alternating domains of Si-enriched britholite and Na-enriched vitusite. Britholite symplectites only occur at 600 °C and have a general orientation perpendicular to the monazite reaction front. The symplectites are not uniform throughout the replacement area. In the proximity of the reaction front next to the monazite, the symplectites are thin and elongated. However they coarsen and form grain clusters in the outer rim of the symplectite.

With respect to fluorapatite, the 600 °C experiments are characterized by extensive formation of britholite, both as an overgrowth as well as a replacement phase. Fig. 12 shows partial pseudomorphic replacement of a fluorapatite crystal with a britholite overgrowth-replacement zone. This zone is further surrounded by vitusite (some of which form euhedral orthorhombic crystals) along with minor britholite intergrowths. The fluorapatite-britholite assemblage reveals a distinct separation between the replacement (Fig. 12a-[a]) and the

overgrowth texture (Fig. 12a-[b]), with nanoporosity development only in the replacement (Fig. 12a inset). In addition, the 600°C experiments are characterized by the presence of an overgrowth boundary enriched in REE creating a BSE light zone around the replacement (Fig. 12a-[b]). The early formed, BSE bright overgrowth gradually evolves into a darker, Ca- and P-enriched, and REE-depleted britholite with well-developed faces. The rim of the britholite overgrowth is characterized by the presence of a few etch pits suggesting the subsequent formation of a direct pathway between the bulk fluid and the fluorapatite grain surface (marked by the red arrow), which is responsible for the development of a broad µm-size intragranular void. The side of the britholite replacement, that is in contact with the intergranular void (Fig. 12b-[c]), exhibits a recrystallization texture, which is suggested by porosity coarsening. In contrast, the porosity of the replacement at the contact with the overgrowth is much finer, with 200 – 500 nm diameter pores, which are more dispersed. Moreover, the well-developed faces on some of the recrystallized, coarse-pore britholite suggest additional britholite crystallization in the intragranular void. In Fig. 13, vitusite precipitation occurred directly within a µm-size void at the fluorapatite-britholite interface, adjacent to an opening in the britholite mantle. Aggressive fluids were first responsible for void formation in the britholite at the contact with the fluorapatite, which allowed for the subsequent crystallization of the pseudo-hexagonal vitusite partially replacing the britholite overgrowth.

Britholite replacement and overgrowth textures were investigated by EMP point analysis, line scans, and element maps. The element maps shown in Fig. 14b-d demonstrate a negative concentration gradient for Ca and P within the britholite replacement outwards, which form elongated "channels" toward the replacement-overgrowth boundary. This is confirmed by

the line scans over the replacement-overgrowth boundary where both Ca and P show decreasing concentration profiles, which extend outwards from the reaction front between the fluorapatite and britholite (Fig. 15). Figure 14c shows an elevated REE content (here using Ce as a proxy) at the replacement-overgrowth boundary corresponding with the brightest zone of the BSE image. Further away, this overgrowth is uniform with a homogeneous element distribution. Concordant EMP point analysis shows that the REE reach their maximum at the replacement-overgrowth boundary. In this area REE_2O_3 reaches its maximum of 58.84 wt%, which is 2 wt% and 8 wt% higher than in the overgrowth and replaced areas, respectively. EMP point analysis suggests that Si and Na also reach their maximums at the boundary between the replacement britholite and the overgrowth britholite (Tab. 2).

Discussion

The results of this experimental study revealed that fluorapatite and monazite show different reaction processes under the P-T conditions covered. The reaction products, pathways, and kinetics have a large temperature dependence. The 300 and 400 °C experiments show variable amounts of monazite replacement and only minor, if any, dissolution of fluorapatite. Under these conditions selective mineral replacement of these phases occurs. The high-temperature 500 and 600 °C experiments are characterized by massive replacement of monazite by vitusite and britholite, as well as substantially more reactive fluorapatite. The latter is both overgrown and pseudomorphically replaced by britholite, wherein oriented nanochannels occur. The

channels are found to contain elevated concentrations of dissolved solutes, and thus are directly related to the process of fluid-mediated, diffusive transport.

Monazite and fluorapatite reactivity and REE mobility in 300 - 400 °C and 100 MPa experiments

The 300 and 400 °C experiments were performed over the same time duration in order to evaluate the influence of temperature on monazite and fluorapatite reactivity and REE mobility. The observed lack of fluorapatite reactivity, together with the sluggish pace of monazite breakdown, as seen in the minor monazite dissolution textures (Figs. 3 & 4), promotes the formation of sazhinite as the low PO_4 and REE phase, and vitusite(Ce) as the Na-bearing phosphate. In nature, vitusite is a rare phase found in highly peralkaline and REE-rich environments. It often forms by the metasomatic interaction of alkaline rocks with late-stage hydrothermal fluids, and has been described as a reaction product during interaction of aqueous fluids with alkaline rocks from the Ilimaussaq Complex, Greenland (Andersen and Sørensen 2005) and with the Lovozero alkaline massif, Russia (Ronsbo et al. 1979; Finch and Fletcher 1992). Sazhinite is a rare Na, REE phyllosilicate, which forms under hyperalkaline conditions, e.g. the Lovozero massif, Mont Saint-Hilaire or the Aris phonolite, Namibia (Cámara et al. 2006). It also forms in hydrothermal or metasomatic paragenesis. The decreasing ratio of sazhinite to vitusite from 300 to 400 °C is indirectly related to the change in monazite solubility.

Increasing the temperature to 400 °C, monazite replacement textures are successively more disrupted, which suggests an enhanced dissolution process causing higher fluxes of REEs

and PO_4 into the bulk fluid. This promotes equal growth between the sazhinite and vitusite, with the latter commonly found associated with the monazite grain surface but occasionally found within the quenched $Na_2Si_2O_5$ glass as isolated crystals. The formation of free vitusite crystals from intragranular fluids can be written as:

$$2(LREE(OH_2)_9^{3+}/(Y+HREE)(OH_2)_8^{3+}) + 4(PO_4)^{3-} + 6Na^+ = 2Na_3(REE)(PO_4)_2 \quad (4)$$

The observed selective reactivity between fluorapatite and monazite is in general accordance with a hypothesis put forward by Rakovan (2013) aiming to explain the unaltered character of the Llallagua fluorapatite, which are surrounded by partially or completely altered monazite grains (Betkowski et al. 2015). This finding may be important in the context of understanding the 20 My age discrepancy, which has been suggested to result from the selective metasomatic alteration of the monazite crystals leading to a bimodal age distribution between Eocene fluorapatite and Miocene monazite identified from the same mineral paragenesis (Rakovan et al. 1997; Kempe et al. 2008; Kohn and Vervoort 2008).

Monazite breakdown and replacement textures at 500°C and 600°C and 100 MPa

A rise in temperature resulted in an increased rate in monazite dissolution. This is evident from the highly evolved monazite dissolution textures despite the shorter length of the experiments (Fig. 5). The enhanced kinetics of monazite dissolution promotes the ubiquitous crystallization of vitusite as replacement after monazite and as free crystals in solution. For some monazite crystals, the britholite corona outlines the initial surface of the dissolving monazite grain and is proposed to form during the beginning of the replacement process (Fig. 5a,b). De Lucas et al.

(2004) showed that a temperature increase correlates with a change in the speciation of $Na_2Si_2O_5$ based fluids. With increasing temperature the solution becomes progressively more silica-saturated by activation of previously inert colloidal silica, which may account for the $Si^{4+} \leftrightarrow P^{5+}$ substitution in the fluorapatite structure according to reaction (2). Other factors which seem to play a role in the development of the britholite coronas include the enhanced kinetics of monazite dissolution, which cause the addition of aqueous REEs into the bulk fluid. The size and shape of the dissolving monazite may dictate if britholite would form as a corona around monazite. For some monazite grains, with greater surface areas undergoing replacement, the change in the ratio between the REE in the solids and the concentration of REE in the boundary fluids may result in local britholite supersaturation forming a corona texture. Development of a britholite corona within the vitusite is used to distinguish between vitusite formed as a result of monazite replacement (Fig. 5b-[1]) and simple overgrowth (Fig. 5b-[2]). Vitusite replacement occurs inward from the britholite corona into the volume formerly occupied by the monazite. Once the replacement reaction is complete, the vitusite may then evolve into a spongy texture, especially in the core zone (Fig. 6). The high density of pores is most likely due to the circulation of fluids throughout the vitusite, which resulted in porosity coarsening; a sort of inverse Ostwald ripening effect.

Exclusively in the 600 °C experiments, monazite replacement takes the form of a symplectite texture riming the partially dissolved monazite grains. They consist of vitusite, which takes the form of a matrix phase, and britholite forming vermicular intergrowths with the matrix (Fig. 11). Traditionally, symplectites have been referred to as a breakdown product in a chemically open-system, which involves mass transfer across a reaction zone (Obata 2011).

Here, symplectite formation utilizes the migration of REEs and Si after vitusite crystallization, which suggests that they formed as a transport related phenomenon with a higher rate of monazite dissolution due to temperature increase. All other factors, including the stability of vitusite and britholite and the proportions of the starting materials, are constant in both the 500 and 600 °C runs.

Formation and evolution of britholite overgrowth and replacement textures around fluorapatite at high temperatures

Both the 500 and 600 °C experiments are characterized by britholite replacement and overgrowth of fluorapatite. Generally, the formation of an overgrowth can be recognized by the development of crystals with distinct facets (Harlov and Hetherington 2010) and the nature of its internal texture. If texturally uncertain, it has been referred to as a replacement-overgrowth zone (Budzyń et al. 2011). In these experiments the overgrowth character of the britholite is deduced by morphological development and chemical zoning with respect to the major elements. Both the overgrowth and replacement britholite are solid solutions between britholite and fluorapatite (i.e. they all have a P component). The britholite-fluorapatite solid solution requires coupled substitutions for charge balance, for which there are several possibilities (with reactions [2] and [3] being the dominant ones). The external morphology of the britholite in Figure 7 suggests overgrowth as seen by the sharp unaltered corners between the crystal faces of fluorapatite and the subhedral habit of the overgrowth. Formation of these britholite-apatite overgrowths can be related to two processes: 1) monazite dissolution and vitusite replacement, which releases significant amounts of REEs into the solution and increases

the relative proportion of Si relative to Na, and 2) dissolution of fluorapatite, which adds P and Ca to solution. The britholite overgrowth in Figure 8a is characterized by concentric zoning. The orientation of the concentric zones in the britholite is parallel to its outer most surfaces, but not conformable with the curvature of the dissolving fluorapatite surface. This is one indicator that the britholite here is an overgrowth and not a replacement of the underlying fluorapatite. The chronological sequence of the concentric zones in the britholite-apatite overgrowth can be used to track temporal changes in the fluid chemistry in the experimental capsules (Fig. 8c,d), which in turn can be understood by the volumetric changes between the reactants and the products. This change also affects which coupled substitution mechanism is dominant in this solid solution. The concentric zones show the gradual transition from REE and Si-dominant britholite into REE+ Na+ Ca and P-dominant fluorapatite. The maximum Si and REE content recorded at the interface with the fluorapatite must reflect the alkalic and silicic fluid conditions during the first days of overgrowth formation. On the other hand, the saturation of a PO_4^- and REE-bearing fluid with vitusite depends mostly on the flux from the volumetrically shrinking monazite during the duration of the experiment. Despite a monazite/fluorapatite molar ratio of 0.7 used in the experiments, monazite, shielded by vitusite, can significantly reduce the available dissolution surface area and thus the activity of REEs in the fluid, which is necessary for vitusite formation. Thus, less vitusite will be formed, which drives up the P fluid concentration and causes the preferential incorporation of P into the britholite-fluorapatite solid solution at the expense of Si. Therefore, the incorporation of the remaining REEs will be coupled with Na substitution via reaction (3) because both occupy the same structural position and are independent of P and Si incorporation.

Other than pure overgrowth, textural and chemical evidence suggest a significant part of the britholite rims was formed as a replacement product of the fluorapatite through the process of coupled dissolution-precipitation (Putnis 2002, 2009). Development of the britholite replacement zone is variable in texture and thickness. The britholite fills the volume and shape of the original fluorapatite, i.e. pseudomorphic replacement, and is characterized by a variable amount of porosity. In the 500 °C experiments, replacement is characterized by a fibrous or wormy britholite partially filling dissolution voids within the fluorapatite (Fig. 9a). This can be understood by considering the local fluid chemistry present at the reaction front similarly to that observed by Xia et al. (2009). The lack of nanoscale coupling is limited by the rate of britholite precipitation. The proximity of other britholite nucleation centers on different fluorapatite crystals, concurrent with the formation of the britholite overgrowths, suggest an insufficient resupply of REEs during the process of monazite breakdown, and subsequent control of local britholite fluid supersaturation.

The 600 °C experiments are characterized by tight fitting replacement with the development of an oriented porosity in the form of nanochannels connecting the reaction front with the surrounding matrix (Fig.12). The replacement of fluorapatite by britholite is accompanied by a minimal (1.1%) negative molar volume change, which may account for the porosity development. However, the observed porosity exceeds that amount, which could be explained by the difference in solubility between the fluorapatite and britholite in the fluids at the reaction front (Putnis 2002, 2009). These textures demonstrate that the nature of the porosity is pervasive, and takes the form parallel nanochannels connecting the reaction front with the fluids present along the replaced mineral grain surface. This finding is important in

understanding the nature of porosity and transport during the replacement process. Previous studies have shown the existence of porosity within areas restricted to the reaction front zone and/or scattered throughout the replacement phase (Harlov et al. 2005; Pöml et al. 2007; Harlov et al., 2010; Harlov and Wirth, 2012;). For most of these studies, there is no clear textural evidence supporting the interconnected nature of the nanoporosity hypothesized for 3-dimensional grains, but not directly visible from 2-dimensional cross sections. The interconnected nanoporosity can be also implied from the presence of a very fine porous microstructure, which does not form a visibly interconnected network (Jonas et al. 2014). This scarcity can be explained in terms of porosity healing and crystal annealing (e.g Harlov et al. 2010). The formation of structurally controlled, elongated nanochannels directly point out existing connections between the bulk fluid and reaction front during the progress of the reaction/replacement front. The coupled dissolution-reprecipitation of fluorapatite is mediated by the degree of fluid reactivity at the reaction front, which greatly relies on the kinetics of a fluid-mediated diffusive transport within a network of nanochannels or an interconnected micro/nanoporosity. In this respect, parameters, such as the dimensions and density of the nanochannels or nanoporosity, will play a primary role in the quantification of transport processes. For fluorapatite-britholite, the replacement nanochannels facilitate the removal of P, Ca, and F into the bulk fluid surrounding the grain and resupply of the reaction front with Si, REE, and Na, which also likely influences pH conditions. The britholite replacement is characterized by enrichment in P and Ca and a substantial decrease in Na compared to the composition of the britholite overgrowth (Fig. 13, Table 2, LAM12-3/II,IV). For the same grain, element mapping (Fig. 14b, d) demonstrates decreasing concentrations of Ca and P outwards

from the fluorapatite towards the overgrowth with parallel nanochannels, which act as mass exchange pathways, and thus drives the fluid-aided diffusion process. Additionally, the prevailing retention of P within the britholite replacement (50%) but with minor Ca (42%) contributes to an incremental change in the P/Ca ratio within the bulk fluid where the overgrowths become REE-fluorapatite during the last stages of growth.

Preservation factors during pseudomorphic fluorapatite replacement

Given that the presence of a structurally controlled porosity within the britholite facilitates fluid exchange during replacement and therefore allows for the progress of the replacement front, any process which can eradicate or block the nanoporosity will stop the progression of the replacement front. Processes for this include the recrystallization of the reprecipitated area, which destroys the existing porosity (Putnis 2009), and the formation of an overgrowth. Textural and chemical data show that the overgrowth not only stops fluorapatite replacement but also helps to preserve the existing replacement structure and mitigate recrystallization. The fluorapatite-britholite replacement shown in Fig. 12a has the characteristics of pseudomorphic replacement of fluorapatite but is overgrown by britholite. The specific timing of overgrowth formation on top of the replacement remains unknown but is suggested to occur syngenetic with britholite replacement and continue as an epigenetic process. The formation of a non-porous britholite overgrowth constitutes an intermediate layer between the bulk fluid and the pseudomorph (zone of britholite replacement). Thus, the formation of an overgrowth is proposed to inhibit or terminate the britholite replacement process. As previously shown, fluids

evolve during the experimental run and become progressively more out of equilibrium (i.e. metastable) with sequentially older mineral replacement products. Here, the formation of an overgrowth acts as a shield protecting the britholite replacement against further alteration or dissolution, which preserves the initial pseudomorphic texture, including the nanoporosity. As indicated by the arrow in Figure 12, an opening, formed by dissolution of a portion of the britholite overgrowth, led to rapid fluid penetration along the britholite-fluorapatite interface. This fluid dissolved some of the fluorapatite along its boundary with the previously formed britholite replacement zone, and also caused some recrystallization (coarsening and removal) of the primary nanoporosity within the britholite replacement. As shown in Figure 12b, nanoporosity is only preserved in areas adjacent to the overgrowth boundary, which had very limited fluid access due to the shielding by the overgrowth on one side, and the recrystallization (coarsening or healing) of nanochannels on the other side. The orientation of fibrous nanochannels within the replacement is constant, regardless of the orientation of the britholite/fluorapatite interface. These are also parallel to the major direction of dissolution and the direction of elongation of the overgrowth crystals. This implies structural control over replacement and overgrowth formation, most likely along the fluorapatite *c*-axis (Rakovan 2002; Elliott 2013). Thus britholite growth (as replacement and overgrowth) must be considered epitaxic, possibly 3D coherent (i.e. topotaxic). If such, the pseudomorphic replacement of fluorapatite by isostructural britholite can be considered as a regenerative mineral replacement because both volume and structure are well preserved across the reaction front. In other words fluorapatite is being coherently replaced by fluorapatite of a different composition, and because of this coherency the replacement is structurally a single crystal rather than polycrystalline.

Fluorapatite-monazite dissolution-replacement coupling mechanism. The implications for multi-phase, simultaneous reaction systems.

Multi-phase reactions are common in nature (Harlov and Förster 2002; Pirajno 2013) and are involved in some experimental studies (e.g Budzyń et al. 2011). They involve reactions where multiple starting phases react to form stable product(s), which is observed in the product assemblage from this experimental study. Although the co-existence of monazite and fluorapatite, with their replacement products, was observed in all the 500 and 600 °C experiments, textural and chemical evidence suggest that equilibrium conditions were not achieved despite the long duration of the experiments. Analysis of the 300 to 600 °C mineral products suggest that multiple reactions drive changes in the fluid-solid equilibrium by modifying the chemical composition of the bulk fluid through enrichment or depletion of various components via a phase specific set of dissolution-precipitation reactions and thus influence the stable mineral paragenesis. The most prominent reactions are two dissolution reactions involving monazite and fluorapatite. Monazite dissolution occurs over all the temperatures covered by this study where the kinetics of dissolution are controlled by temperature increase. Fluorapatite remains intact at 300 °C, and insignificantly dissolved at 400 °C, but significantly reactive at 500 and 600 °C (Fig.2). Three phases formed during these experiments: sazhinite, which is found only at 300 and 400 °C, britholite, which is found at 400 to 600 °C, and vitusite. Vitusite is the most widespread reaction phase, which mainly forms as a monazite replacement product but also grows freely into the solution. In a low pressure, $Na_2Si_2O_5$-rich fluid environment, vitusite replacement after monazite leads to an increase in the

amount of REEs supplied into the fluid. Vitusite crystallization within the capsule decreases the REE and PO_4 concentration, which enhances further dissolution of monazite and fluorapatite by maintaining the disequilibrium state between the fluids and solids. On the other hand, fluorapatite dissolution and britholite replacement add Ca and P into the intragranular bulk fluids (see above). Formation of britholite overgrowths was observed to have a positive effect on both the fluorapatite and monazite reactivity. Britholite overgrowth formation decreases Ca, P, and REE concentration in solution, which enhances fluorapatite and monazite dissolution. This chain of reactions forms a coupled fluorapatite-monazite dissolution system, which, in conjunction with crystallization of britholite and vitusite, buffers the fluid reactivity and drives the bulk re-equilibration beyond the extent of one-phase, fluid-solid interactions. This coupling also acts against the regenerative dissolution-precipitation of monazite since the fluids are never enriched to the point necessary for monazite regenerative replacement like that presented in Harlov et al. 2010.

There are three factors, which influence the termination of this self-perpetuating reaction: 1) consumption of all the reactants; 2) armoring the reactants which mitigate fluid exchange; and 3) the consumption of monazite. The latter would stop the supply of REEs to the solution and thus the formation of britholite. This was observed in the chemistry of the overgrowth rims and textures formed as a result of reactant deficiency during the latter days of experimental runs (Fig. 8).

Implications

The experiments reported here are the first, which focus on the investigation of the simultaneous reactivity of fluorapatite and monazite. It reveals a coupling between their reactivities, which points to a prolonged bulk re-equilibration beyond the extent of one-phase-only fluid-solid interactions. The high-temperature 500 and 600 °C experiments are characterized by reactivity of both the monazite and the fluorapatite, which are replaced by vitusite and britholite, respectively. The nature of these replacements gives us insight into the range of structural and chemical fidelities between the reactant and product phases during pseudomorphism. In the case of vitusite replacement of monazite, only gross fidelity to the original monazite morphology is achieved, which is delineated by the observed corona textures. In this case, as with most pseudomorphism, the product phase is polycrystalline. The mechanism of spatially and temporally coupled dissolution-precipitation, which is responsible for the fluorapatite replacement, is shown to rely on the formation of oriented nanochannels, which facilitate fluid-based mass transfer across the replaced fluorapatite. The resulting pseudomorphic formation of isostructural britholite can be thought of as an example of regenerative mineral replacement, wherein structural as well as morphologic fidelity is achieved.

This experimental study shows that fluorapatite and monazite show different reactivities in Na and Si-rich aqueous fluids at 300 – 400 °C and 100 MPa. Monazite and fluorapatite are among some of the most important geochronometers. Interpretation of dates determined by geochronologic analysis of these minerals is dependent on their thermal, chemical, and structural histories. Many examples exist, for each of these minerals, where geological events have altered their chemistry and or structure such that extracted dates do not represent their

age, but rather the age of the modifying event (e.g Harrison et al. 2002). The key to dating the age of these minerals, and the rocks that host them, is to understand the conditions under which their alteration occurred, and know how to decipher if such alteration has occurred. The selective reactivity of fluorapatite and monazite may then lead to geochronologic discrepancies, when they are found together (e.g. at Llallagua), which can only be understood if the conditions for this selectivity are known.

Both monazite and fluorapatite have been the focus of intensive study as potential solid nuclear waste forms (Ewing and Wang 2002). The observed differential reactivity of these phases may have important implications for their use in this application. The differential reactivity indicates that the choice of an appropriate waste form must take into consideration the possible geologic fluids that the waste form is likely to interact with. Fluids with other geologically relevant chemistries and conditions should be investigated for a broader understanding of the differential reactivity of these two phases over the same P-T range.

Acknowledgements

We would like to thank Dieter Rhede of the GeoForschungsZentrum, Potsdam, for his expertise with the electron microprobe and helpful comments. Richard Edelman and Mat Duley are thanked for assistance with the SEM. We thank Jaroslaw Majka and an anonymous reviewer for their insightful comments on an earlier version on this manuscript. Support for this work was provided by the National Science Foundation through grant EAR-0952298 to JR.

References

Andersen, T., and Sørensen, H. (2005) Stability of naujakasite in hyperagpaitic melts, and the petrology of naujakasite lujavrite in the Ilímaussaq alkaline complex, South Greenland. Mineralogical Magazine, 69, 125–136.

Betkowski, W., Rakovan, J., and Harlov, D. (2015) Monazite, Xenotime and Apatite Chemistry and Textures: Clues to Understanding Geochronologic Discrepancies in the Llallagua Tin Deposit, Bolivia. In Goldschmidt Abstracts p. 283.

Bhowmik, S.K., Wilde, S.A., Bhandari, A., and Basu Sarbadhikari, A. (2014) Zoned Monazite and Zircon as Monitors for the Thermal History of Granulite Terranes: an Example from the Central Indian Tectonic Zone. Journal of Petrology, 55, 585–621.

Budzyń, B., Harlov, D.E., Williams, M.L., and Jercinovic, M.J. (2011) Experimental determination of stability relations between monazite, fluorapatite, allanite, and REE-epidote as a function of pressure, temperature, and fluid composition. American Mineralogist, 96, 1547–1567.

Cámara, F., Ottolini, L., Devouard, B., Garvie, L.A.J., and Hawthorne, F.C. (2006) Sazhinite-(La), Na3LaSi6O15(H2O)2, a new mineral from the Aris phonolite, Namibia: Description and crystal structure. Mineralogical Magazine, 70, 405–418.

Chew, D.M., and Spikings, R.A. (2015) Geochronology and thermochronology using apatite: time and temperature, lower crust to surface. Elements, 11, 189–194.

Elliott, J.C. (2013) Structure and chemistry of the apatites and other calcium orthophosphates. Elsevier.

Ewing, R.C., and Wang, L. (2002) Phosphates as nuclear waste forms. Reviews in mineralogy and geochemistry, 48, 673–699.

Finch, A.A., and Fletcher, J.G. (1992) Vitusite — An Apatite Derivative Structure. Mineralogical Magazine, 56, 235–239.

Grant, J.N., Halls, C., Sheppard, S.M.F., and Avila, W. (1980) Evolution of the Porphyry Tin Deposits of Bolivia. Mining Geology Special Issue, 8, 151–173.

Harlov, D.E. (2015) Apatite: A Fingerprint for Metasomatic Processes. Elements , 11 , 171–176.

Harlov, D.E., and Förster, H.-J. (2002) High-Grade Fluid Metasomatism on both a Local and a Regional Scale: the Seward Peninsula , Alaska , and the Val Strona di Omegna , Ivrea – Verbano Zone , Northern Italy . Part II: Phosphate Mineral Chemistry. Jurnal of Petrology, 43, 801–824.

Harlov, D.E., and Förster, H.-J. (2003) Fluid-induced nucleation of (Y+REE) -phosphate minerals within apatite: Nature and experiment . Part II . Fluorapatite. American Mineralogist, 88, 1209–1229.

Harlov, D.E., and Hetherington, C.J. (2010) Partial high-grade alteration of monazite using alkali-bearing fluids: Experiment and nature. American Mineralogist, 95, 1105–1108.

Harlov, D.E., and Wirth, R. (2012) Experimental incorporation of Th into xenotime at middle to lower crustal P-T utilizing alkali-bearing fluids. American Mineralogist, 97, 641–652.

Harlov, D.E., Wirth, R., and Förster, H.-J. (2005) An experimental study of dissolution–reprecipitation in fluorapatite: fluid infiltration and the formation of monazite. Contributions to Mineralogy and Petrology, 150, 268–286.

Harlov, D.E., Wirth, R., and Hetherington, C.J. (2010) Fluid-mediated partial alteration in monazite: the role of coupled dissolution–reprecipitation in element redistribution and mass transfer. Contributions to Mineralogy and Petrology, 162, 329–348.

Harrison, T.M., Catlos, E.J., and Montel, J.-M. (2002) U-Th-Pb Dating of Phosphate Minerals. Reviews in Mineralogy and Geochemistry, 48, 524–558.

Hughes, J.M., and Rakovan J.F (2015) Structurally Robust, Chemically Diverse: Apatite and Apatite Supergroup Minerals. Elements: 11, 165-170.

Jarosewich, E., and Boatner, L.A. (1991) Rare-Earth Element Reference Samples for Electron Microprobe Analysis. Geostandards Newsletter, 15, 397–399.

Jonas, L., John, T., King, H.E., Geisler, T., and Putnis, A. (2014) The role of grain boundaries and transient porosity in rocks as fluid pathways for reaction front propagation. Earth and Planetary Science Letters, 386, 64–74.

Kelly, W.C., and Turneaure, F.S. (1970) Mineralogy, paragenesis and geothermometry of the tin and tungsten deposits of the eastern Andes, Bolivia. Economic Geology, 65, 609–680.

Kempe, U., Lehmann, B., Wolf, D., Rodionov, N., Bombach, K., Schwengfelder, U., and Dietrich, A. (2008) U–Pb SHRIMP geochronology of Th-poor, hydrothermal monazite: An example from the Llallagua tin-porphyry deposit, Bolivia. Geochimica et Cosmochimica Acta, 72, 4352–4366.

Kohn, M.J., and Vervoort, J.D. (2008) U-Th-Pb dating of monazite by single-collector ICP-MS: Pitfalls and potential. Geochemistry, Geophysics, Geosystems, 9, 1–16.

Kontak, D.J., and Clark, A.H. (2002) Genesis of the Giant, Bonanza San Rafael Lode Tin Deposit, Peru: Origin and significance of pervasive alteration. Economic Geology, 97, 1741–1777.

Kusiak, M.A., Williams, I.S., Dunkley, D.J., Konečny, P., Słaby, E., and Martin, H. (2014) Monazite to the rescue: U-Th-Pb dating of the intrusive history of the composite Karkonosze pluton, Bohemian Massif. Chemical Geology, 364, 76–92.

Obata, M. (2011) Kelyphite and symplectite: textural and mineralogical diversities and universality, and a new dynamic view of their structural formation. INTECH Open Access Publisher.

Pan, Y., and Fleet, M.E. (2002) Compositions of the apatite-group minerals: substitution mechanisms and controlling factors. Reviews in Mineralogy and Geochemistry, 48, 13–49.

Pirajno, F. (2013) Effects of metasomatism on mineral systems and their host rocks: alkali metasomatism, skarns, greisens, tourmalinites, rodingites, black-wall alteration and listvenites. Metasomatism and the Chemical Transformation of Rock . Springer, 203–251.

Pöml, P., Menneken, M., Stephan, T., Niedermeier, D.R.D., Geisler, T., and Putnis, A. (2007)

Mechanism of hydrothermal alteration of natural self-irradiated and synthetic crystalline titanate-based pyrochlore. Geochimica et Cosmochimica Acta, 71, 3311–3322.

Putnis, A. (2002) Mineral replacement reactions: from macroscopic observations to microscopic mechanisms. Mineralogical Magazine, 66, 689–708.

Putnis, A. (2009) Mineral Replacement Reactions. Reviews in Mineralogy and Geochemistry, 70, 87–124.

Rakovan, J.F. (2002) Growth and Surface Properties of Apatite. Reviews in Mineralogy and Geochemistry, 48, 51–86.

Rakovan, J.F. (2013) Apatite and other phosphates from Llallagua, Bolivia: An interesting story of hydrothermal mineralization and pseudomorphism. Rochester Mineralogical Symposium Program with Abstracts.

Rakovan, J.F. McDaniel, D.K., and Reeder, R.J. (1997) Use of surface-controlled REE sectoral zoning in apatite from Llallagua, Bolivia, to determine a single-crystal Sm-Nd age. Earth and Planetary Science Letters, 146, 329–336.

Rapp, R.P., and Watson, E.B. (1986) Monazite solubility and dissolution kinetics: implications for the thorium and light rare earth chemistry of felsic magmas. Contributions to Mineralogy and Petrology, 94, 304–316.

Ronsbo, J.G., Khomyakov, A.P., Semenov, E.I., Voronkov, A.A., and Garanin, V.K. (1979) Vitusite—A New Phosphate of Sodium and Rare Earths from the Lovozero Alkaline Massif, Kola, and the Ilimaussaq Alkaline Intrusion, South Greenland. Jurnal of Mineralogy and Geochemistry, 137, 42–53.

Schettler, G., Gottschalk, M., and Harlov, D.E. (2011) A new semi-micro wet chemical method for apatite analysis and its application to the crystal chemistry of fluorapatite-chlorapatite solid solutions. American Mineralogist, 96, 138–152.

Sillitoe, R.H., Halls, C., and Grant, J.N. (1975) Porphyry Tin Deposits in Bolivia. Economic Geology, 70, 913–927.

Stormer, J., Pierson, M.L., and Tacker, R.C. (1993) Variation of F and Cl X-ray intensity due to anisotropic diffusion in apatite. American Mineralogist, 78, 641–648.

Sugaki, A., Kojima, S., and Shimada, N. (1988) Fluid inclusion studies of the polymetallic hydrothermal ore deposits in Bolivia. Mineralium Deposita, 15, 9–15.

Torab, F.M., and Lehmann, B. (2007) Magnetite-apatite deposits of the Bafq district, Central Iran: apatite geochemistry and monazite geochronology. Mineralogical Magazine, 71, 347–363.

Tropper, P., Manning, C.E., and Harlov, D.E. (2013) Experimental determination of CePO4 and YPO4 solubilities in H2O–NaF at 800° C and 1 GPa: implications for rare earth element transport in high-grade metamorphic fluids. Geofluids, 13, 372–380.

Williams, M.L., Jercinovic, M.J., Harlov, D.E., Budzyń, B., and Hetherington, C.J. (2011) Resetting monazite ages during fluid-related alteration. Chemical Geology, 283, 218–225.

Xia, F., Brugger, J., Chen, G., Ngothai, Y., O'Neill, B., Putnis, A., and Pring, A. (2009) Mechanism

and kinetics of pseudomorphic mineral replacement reactions: A case study of the replacement of pentlandite by violarite. Geochimica et Cosmochimica Acta, 73, 1945–1969.

Figure Captions

Figure 1 SEM-BSE images of unreacted grains used in experiments. a) synthetic fluorapatite (FAp) b) Llallagua fluorapatite with visible zoning pattern c) Llallagua monazite (Mnz) d) synthetic monazite.

Figure 2 BSE-SEM images of fluorapatite (FAp) crystals reacted with alkali-fluids, in the absence of monazite. a) 300 °C, 100 MPa, experiment LAM5 b) 400 °C, 100 MPa, experiment LAM6. Note the small dissolution pits along the top edge of the crystal c) 500 °C, 100 MPa, experiment LAM7. The parallel dissolution pits visible from the top of fluorapatite crystal are associated with F-depleted replacement zones (see arrow) that extend past the end of the pits. d) 600 °C, 100 MPa, experiment LAM8. In the heavily etched fluorapatite crystal dissolution channels are parallel probably indicating the *c*-axis direction.

Figure 3 BSE-SEM images of experiment LAM9 (300 °C, 100 MPa) products. Natural Llallagua monazite (Mnz) partially replaced by vitusite (Vts). Unlike experiments with synthetic monazite, the uneven Llallagua monazite reaction front may be the result of structural defects, which increase the lattice strain and thus locally promote the dissolution within the grain. FAp - fluorapatite, Szh - sazhinite.

Figure 4 400 °C, 100 MPa, experiment LAM10. SEM-BSE image of partially pseudomorphically replaced monazite (Mnz) by vitusite (Vts). Both monazite and vitusite are overgrown by sazhinite which armors the monazite crystal. The inset magnifies the segment of monazite replacement, which is not completely armored by sazhinite. This facilitates free access of fluids into monazite surface. Szh - sazhinite.

Figure 5 BSE-SEM image of monazite (Mnz) partially replaced by vitusite (Vts) with formation of a britholite (Brt) corona texture. a) 500 °C 100 MPa, experiment LAM3. b) LAM11 500 °C, 100 MPa. The early formed britholite corona (the red dashed line) outlines the initial shape of the monazite crystal and is followed by vitusite replacement of monazite and in some cases additional overgrowth by vitusite.

Figure 6 500 °C, 100 MPa, experiment LAM11. BSE-SEM image shows two stages of monazite (Mnz) replacement by vitusite (Vts). Left: monazite is partially altered into vitusite and surrounded by a fine-grained britholite corona. Right: vitusite is a complete product of monazite replacement with significant porosity development. Note that there are fragments of unaltered monazite [a] and minute britholite (Brt) [b] embedded in the replacement vitusite.

Figure 7 500 °C, 100 MPa, experiment LAM11. BSE-SEM image of an fluorapatite (FAp) overgrown by britholite (Brt). Britholite is armoring the fluorapatite, preventing reaction with the bulk fluid. Vts - vitusite.

Figure 8 500 °C, 100 MPa, experiment LAM3. a) BSE-SEM image of a britholite (Brt) forming a zoned overgrowth around a BSE black fluorapatite (FAp) core. LS-1 - WDS line scan no.1, LS-2 - WDS line scan no.2. The green rectangular area is magnified on Fig. 7b b) Dark line is a burn trace from the microprobe line scan. Dashed circles indicate areas of microprobe point analysis c) X-ray intensity plot over line scan no.1. d) X-ray intensity plot over line scan no.2. Elements showed: Na(black), Ce(green), Ca(purple), Si(red), P(blue).

Figure 9 500 °C, 100 MPa, experiment LAM11. a) BSE-SEM image of mixed overgrowth-replacement texture around a fluorapatite (FAp). [1] ~20 µm thick uniform layer of britholite (Brt) overgrowth. [2] Fibrous britholite replacement of fluorapatite that partially fills a pore space after fluorapatite dissolution. The red square indicates the area showed on x-ray maps that clearly delineate the overgrowth and replacements with a sharp compositional boundary. b) X-ray map of phosphorous c) cerium d) silicon e) sodium.

Figure 10 500 °C, 100 MPa, experiment LAM11. BSE-SEM image of mixed overgrowth-replacement texture around fluorapatite (FAp). Britholite (Brt) replacement is characterized by tight filling of space after fluorapatite dissolution which is accompanied by formation of parallel nanochannels [1]. Adjacent to the britholite replacement, britholite overgrowth is free of elongate nanoporosity [2].

Figure 11 600 °C, 100 MPa, experiment LAM4. BSE-SEM image of monazite (Mnz) replacement texture that consists of a vitusite-britholite symplectite. The symplectite originates at the monazite reaction front and comprises vermicular grains of Si-enriched britholite (Brt) embedded within vitusite (Vts).

Figure 12 600 °C, 100 MPa, experiment LAM12. BSE-SEM image of fluorapatite (FAp) replacement assemblage. a) BSE-dark, centrally situated fluorapatite is partially, pseudomorphically replaced by nanoporous britholite (Brt-rpl) [a]. This zone is further mantled by britholite overgrowth (Brt-ovg) [b]. The fluorapatite overgrowth is mainly surrounded by vitusite crystals, intergrown with minute britholite grains. An inset magnifies the nanoporosity formed within the britholite replacement zone. b) Coarsening and recrystallization of nanoporosity within a replacement zone. Very limited scattered, coarse porosity is observed in the proximity of the void between the fluorapatite and the replacement zone [c]. Significantly more nanopores occupy the space directly adjacent to the overgrowth boundary [d].

Figure 13 600 °C, 100 MPa, experiment LAM12. BSE-SEM image of a britholite replacement-overgrowth zone around the fluorapatite (FAp). Britholite (Brt) replacement is characterized by development of a linear nanoporosity and darker BSE contrast. An overgrowth is BSE brighter due to a higher REE content. Orange spheres are marking spots for EMP point analysis. Red box

indicates an area of x-ray maps shown in Figure 14. Blue box marks the region magnified in the inset and shows the contact between replacement and overgrowth. The dashed blue line indicates the location of an X-ray line scan plotted in Figure 15. Vts - vitusite.

Figure 14 a) The SEM-BSE image of an area marked by a red box in Figure 13 showing overgrowth-replacement zone around a fluorapatite (FAp) b) X-ray map of Calcium c) Cerium d) Phosphorous. The separation between the replacement (Brt-rpl) and overgrowth (Brt-ovg) zones is visible through both textural and chemical characteristics (e.g. development of nanoporosity with replacement, REE-rich overgrowth, tracks of Ca and P chemical gradients within replacement). Vts - vitusite.

Figure 15 Electron microprobe line scans over replacement-overgrowth boundary around fluorapatite crystal showed in Figure 13. Dashed black lines mark characteristic transition points: fluorapatite-reaction front-britholite replacement (left), britholite replacement-britholite overgrowth (right). Comparing with replacement, britholite overgrowth is characterized by substantial increase in REE, Na and Si.

Tables

Tables are attached in Microsoft Excel format as a separate file.

Figures

Figure 1

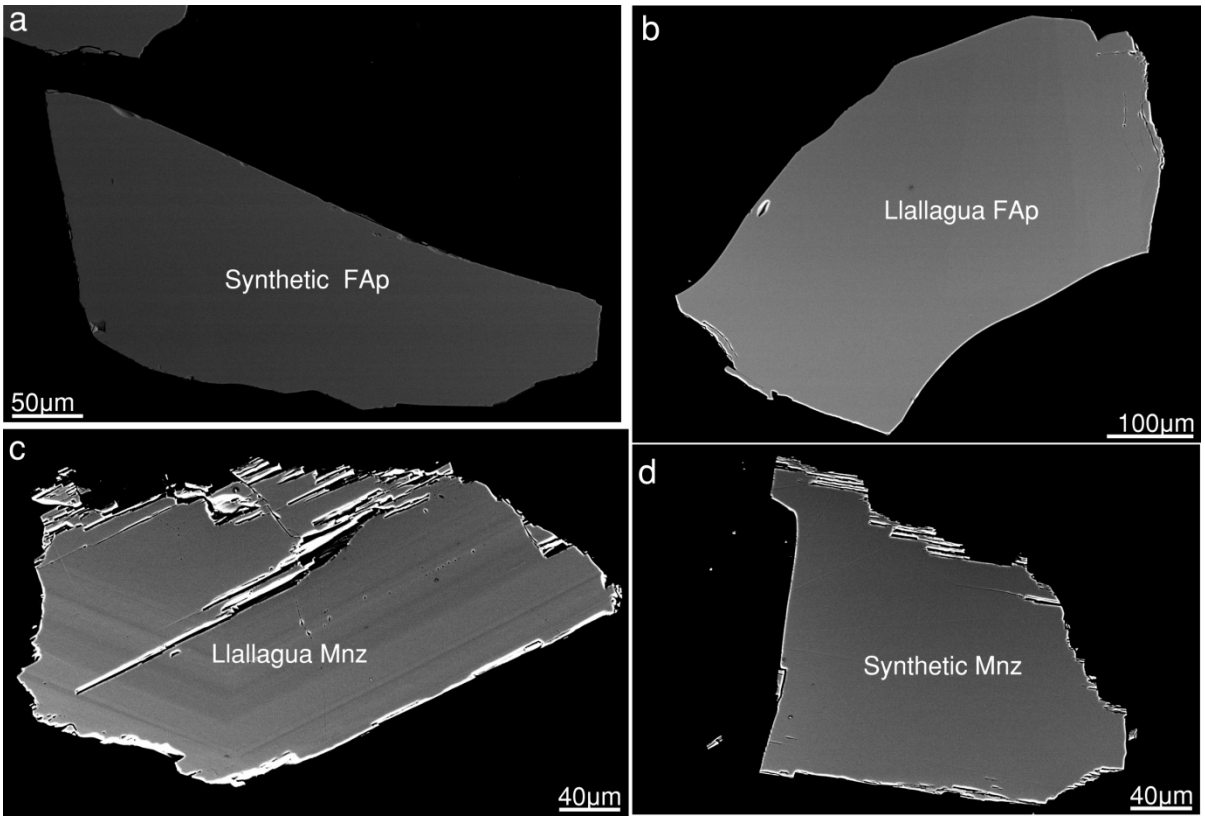
a
Synthetic FAp
50µm
b
Llallagua FAp
100µm
c
Llallagua Mnz
40µm
d
Synthetic Mnz
40µm

Figure 2

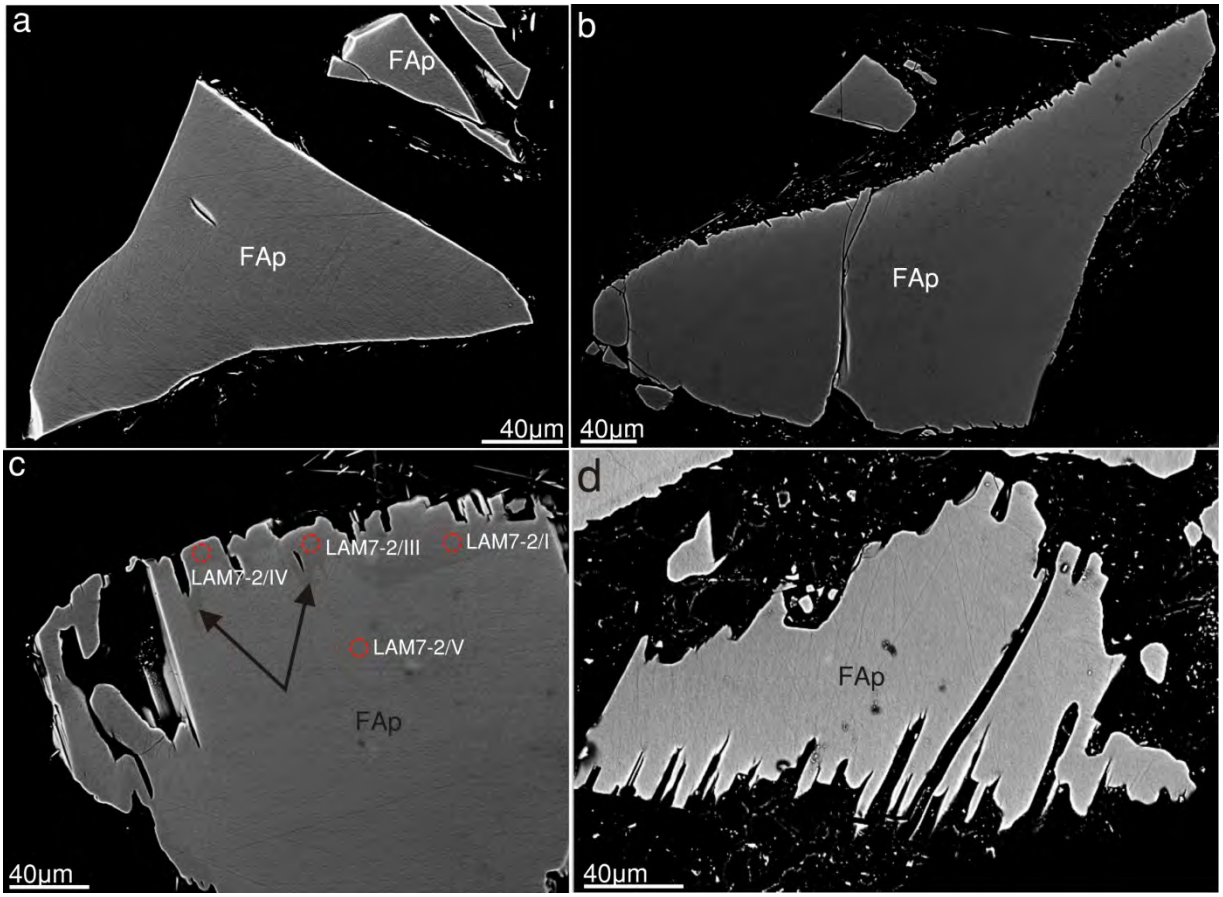

Figure 3

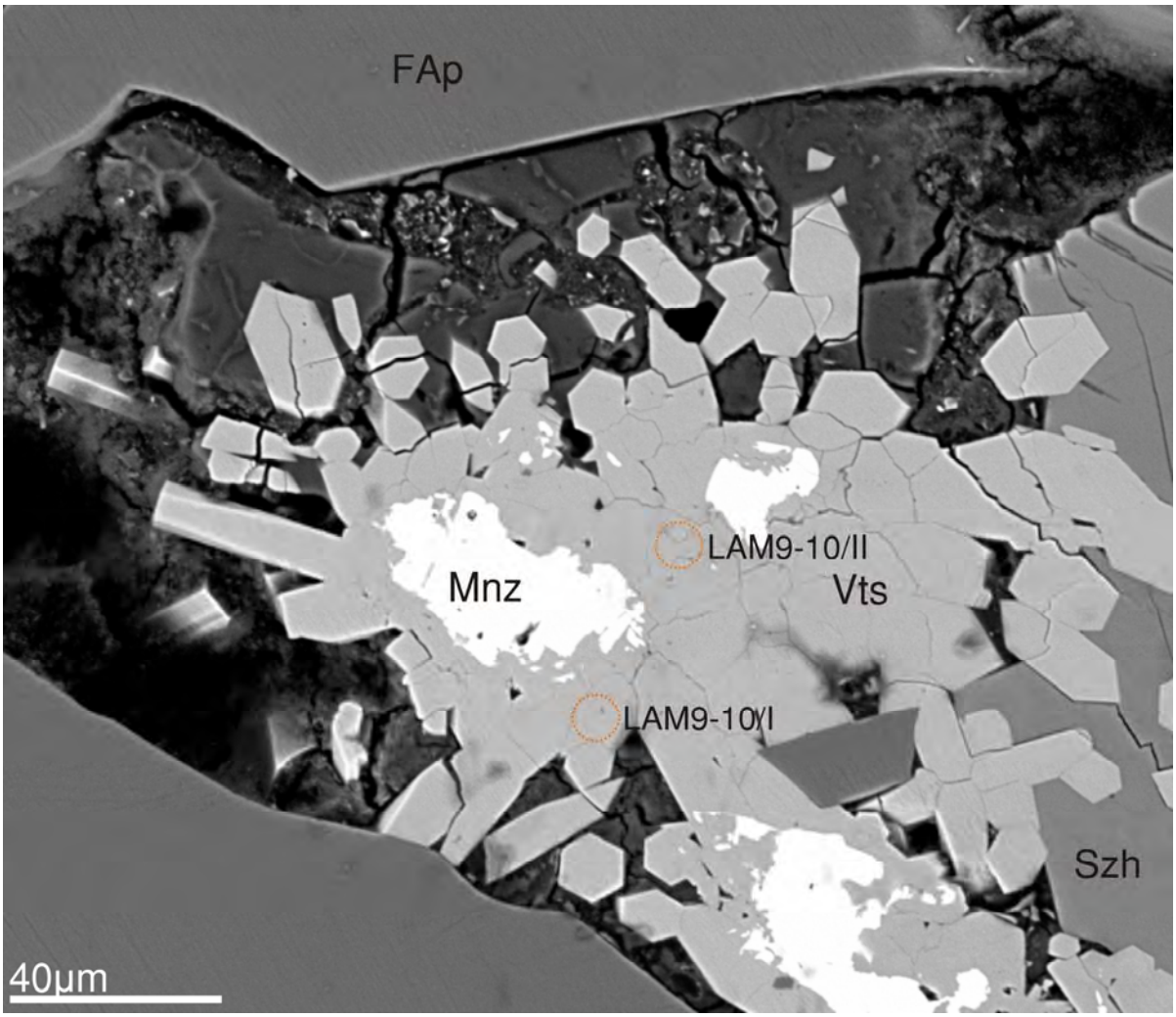

Figure 4

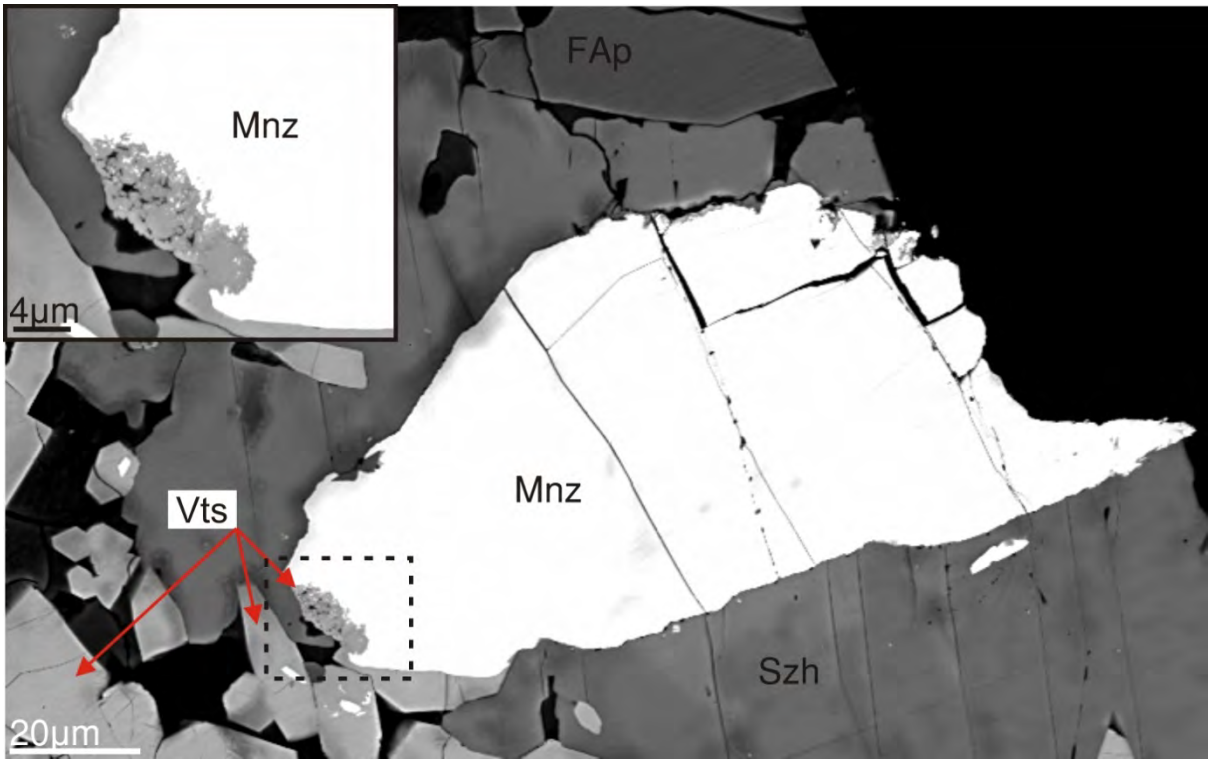

Figure 5

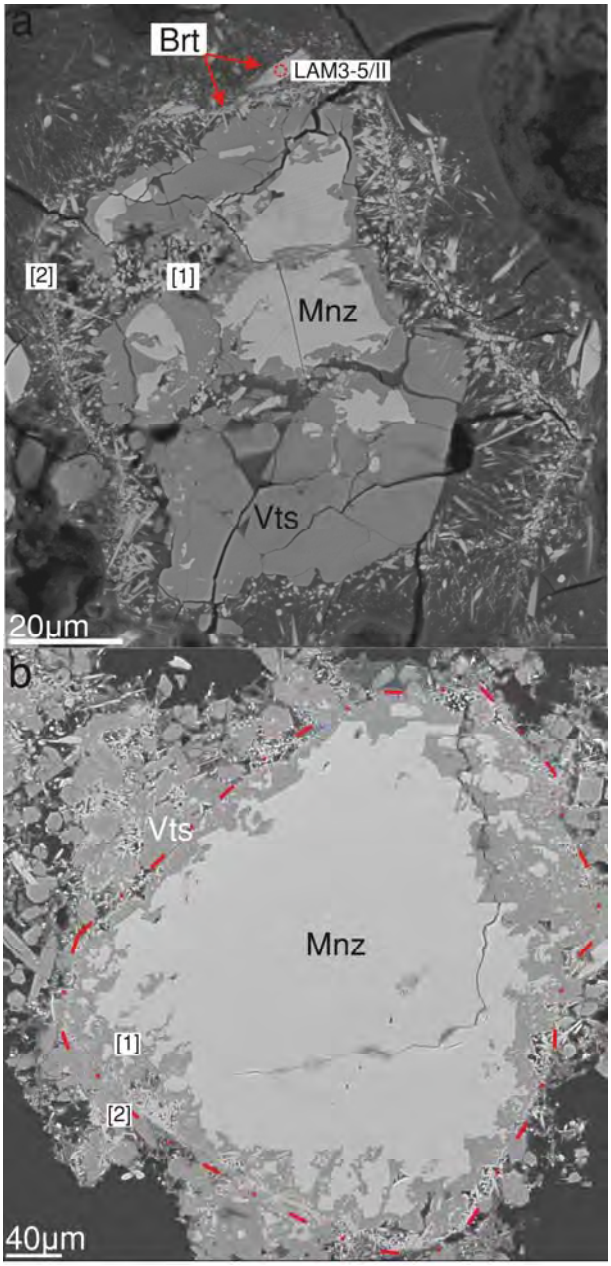

Figure 6

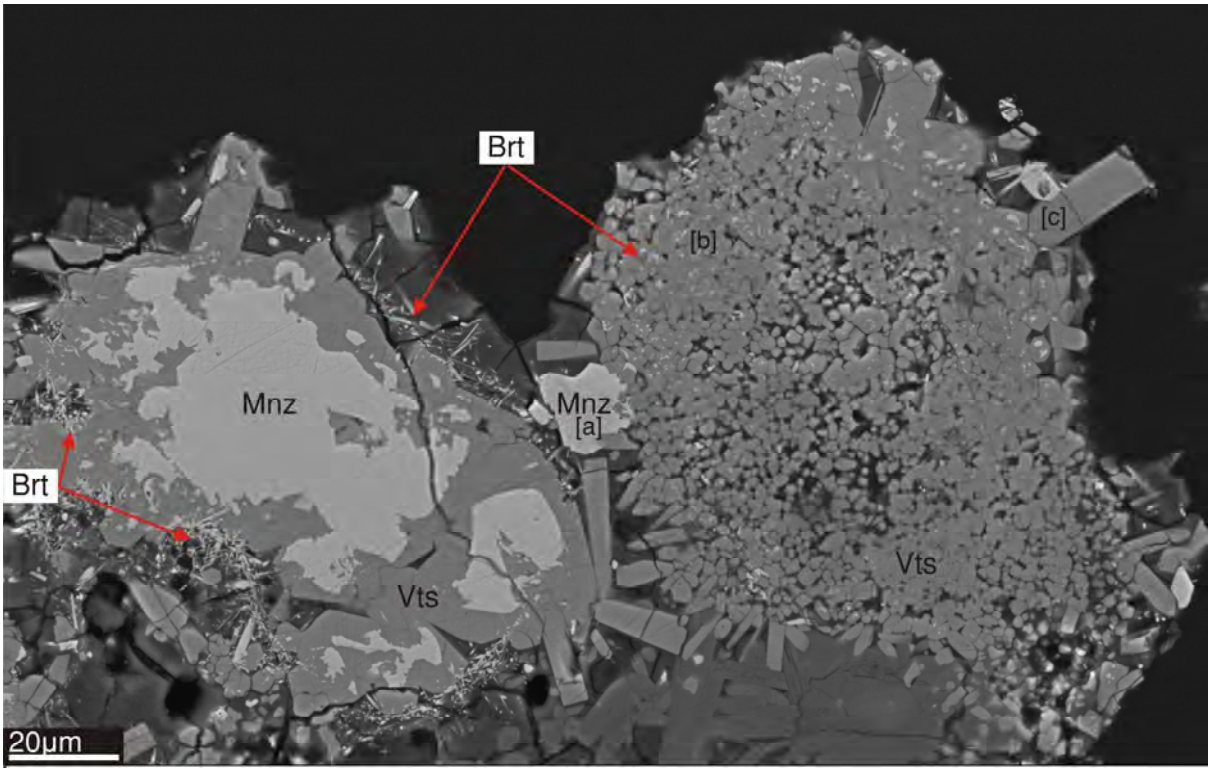

Figure 7

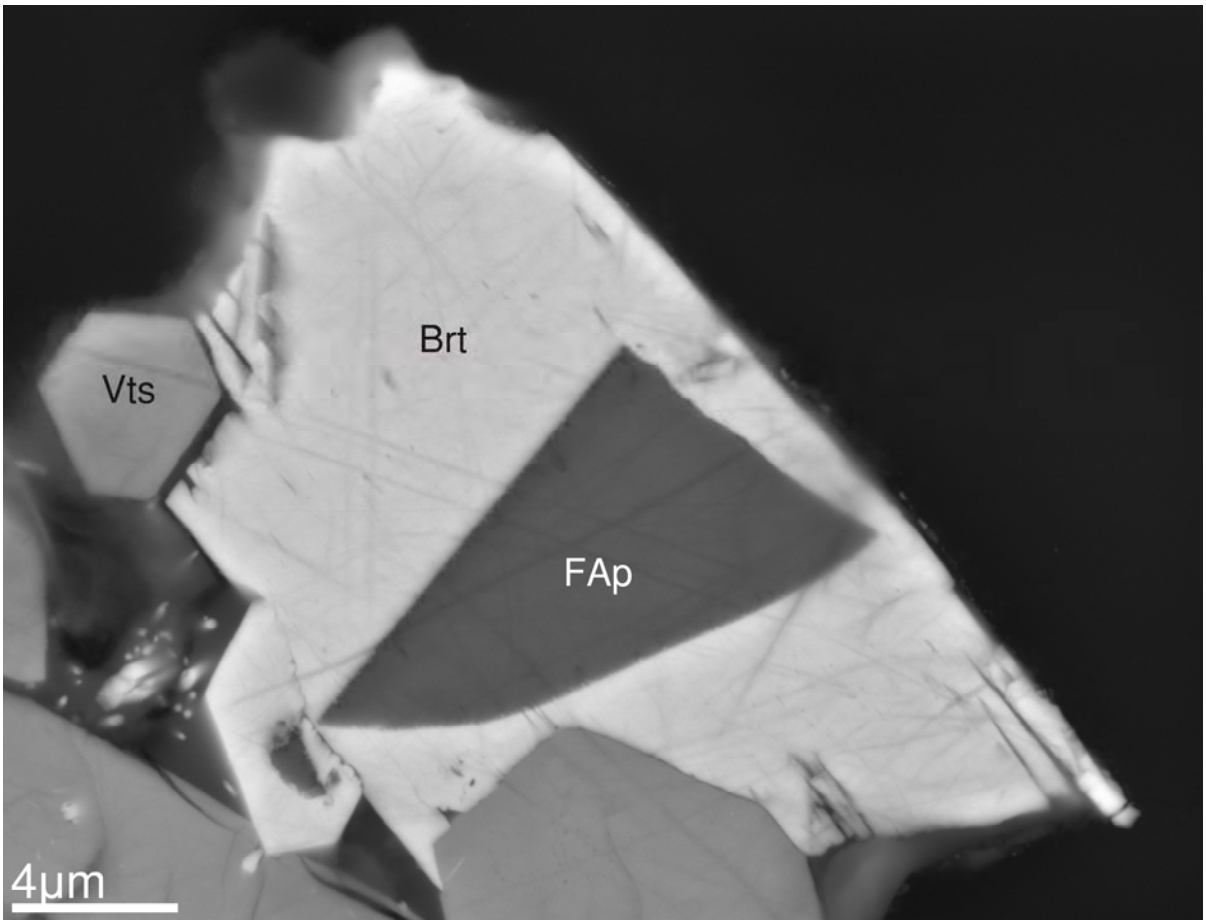

Figure 8

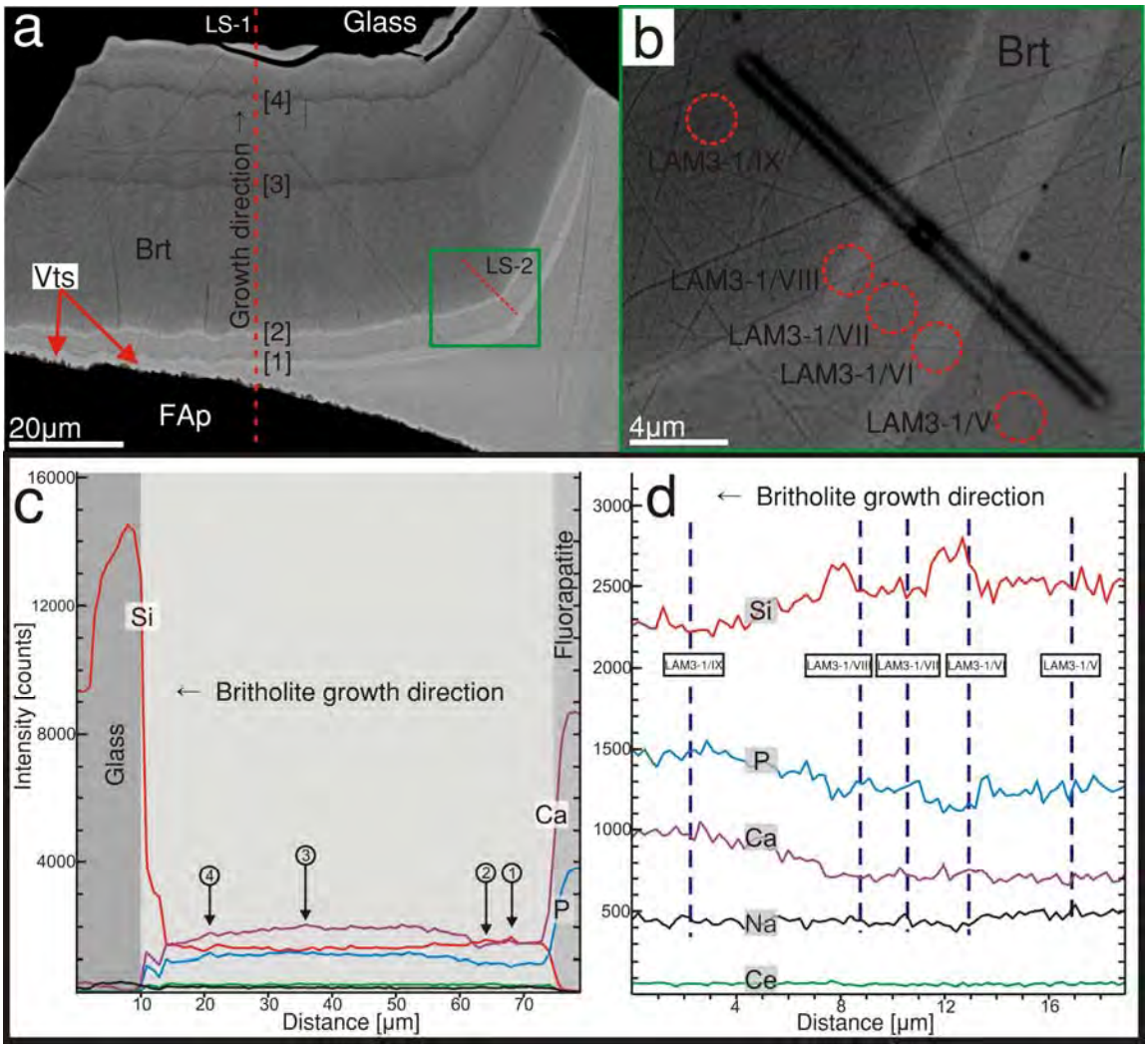
a
LS-1
Glass
[4]
[3]
Growth direction
Brt
Vts
LS-2
[2]
[1]
FAp
20µm
b
Brt
LAM3-1/IX
LAM3-1/VIII
LAM3-1/VII
LAM3-1/VI
LAM3-1/V
4µm
c
Intensity [counts]
Si
Glass
← Britholite growth direction
Fluorapatite
Ca
P
Distance [µm]
d
← Britholite growth direction
Si
P
Ca
Na
Ce
Distance [µm]

Figure 9

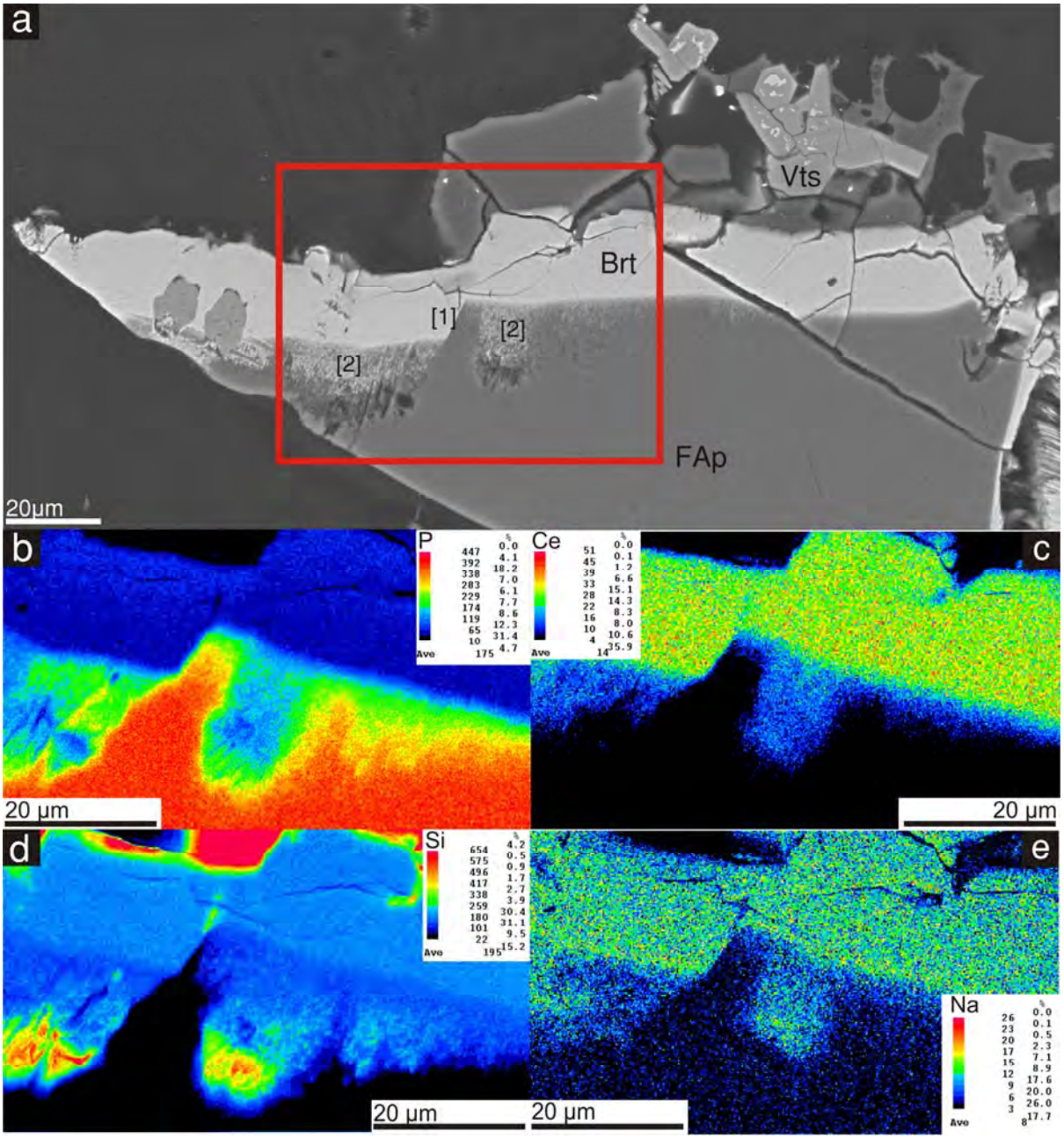

Figure 10

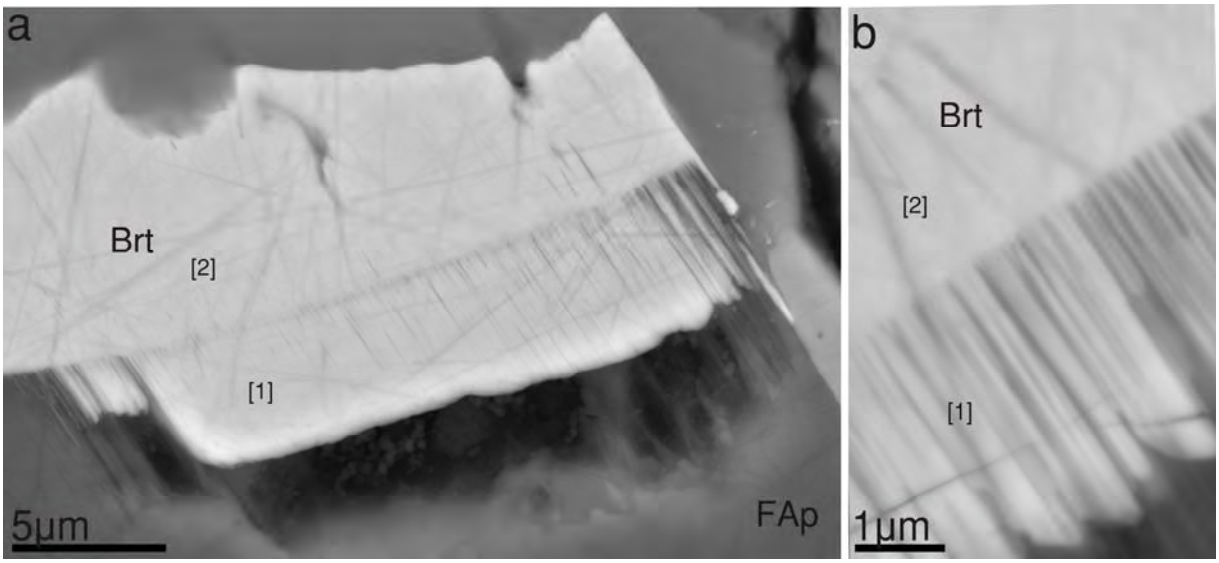

Figure 11

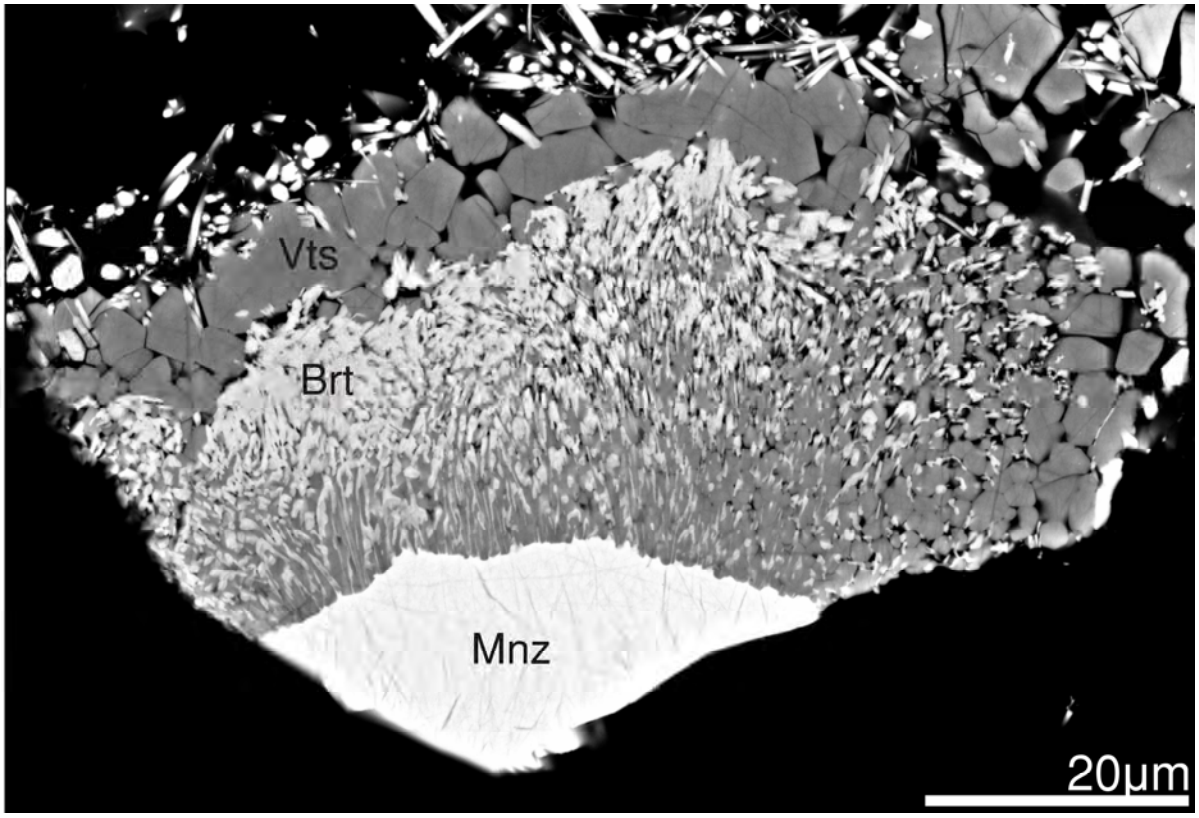

Figure 12

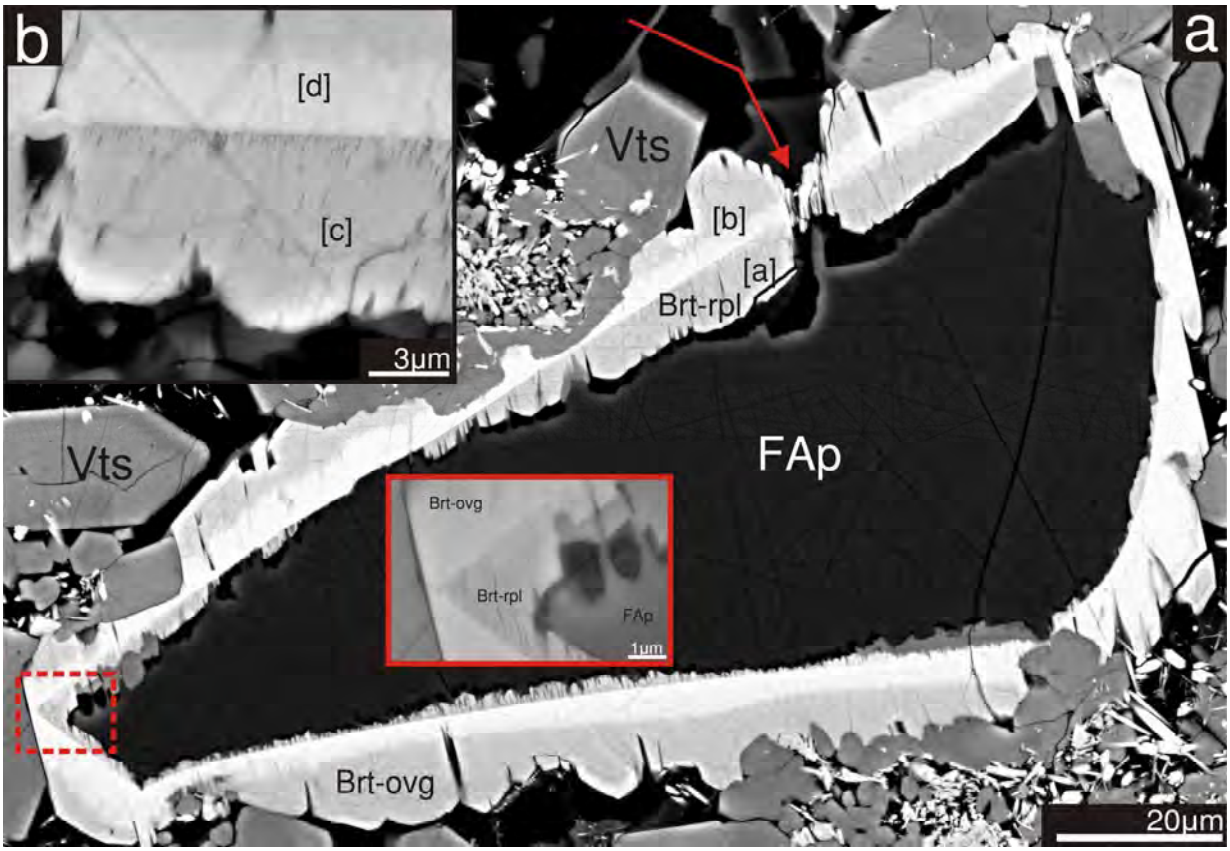

Figure 13

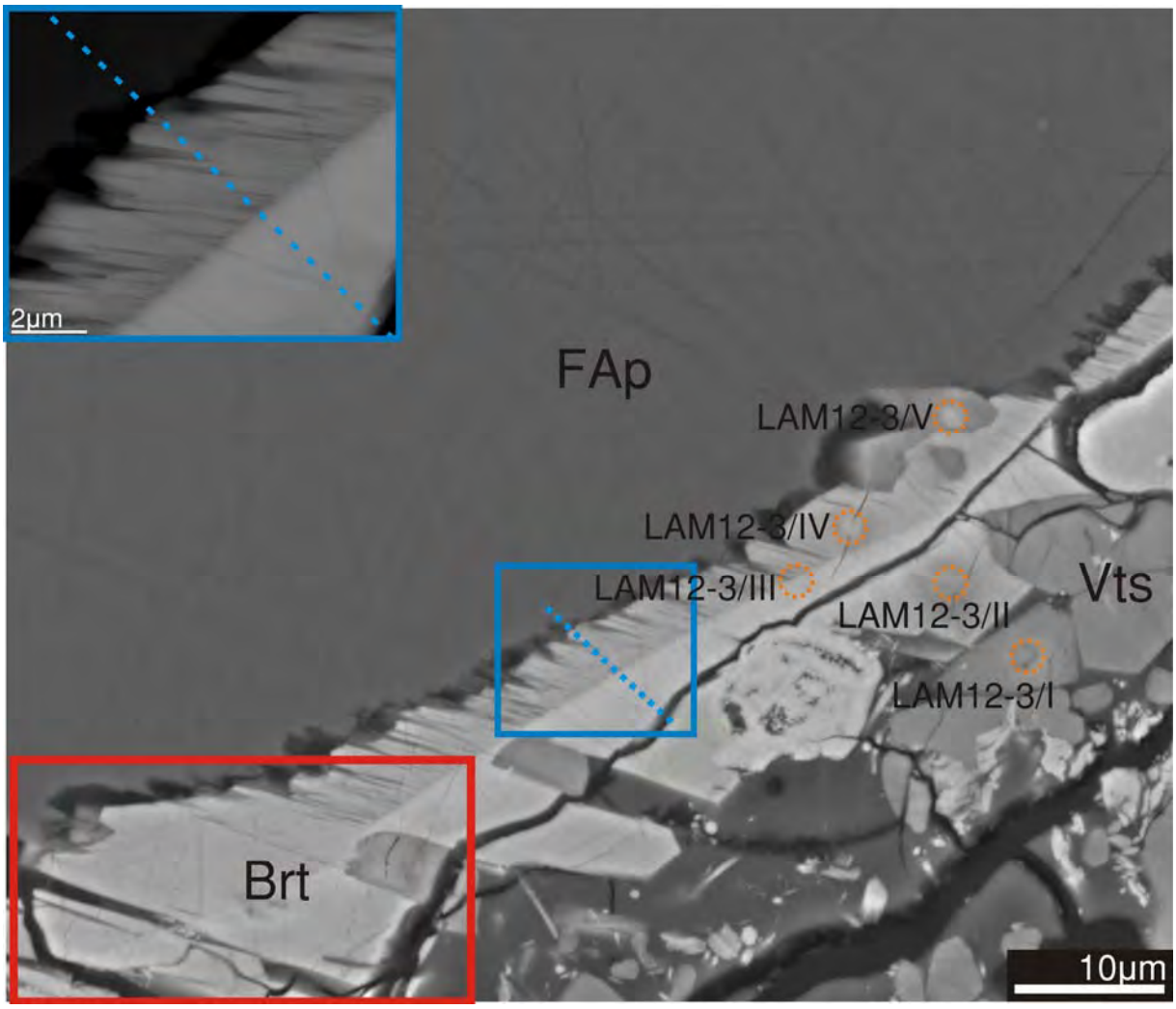

Figure 14

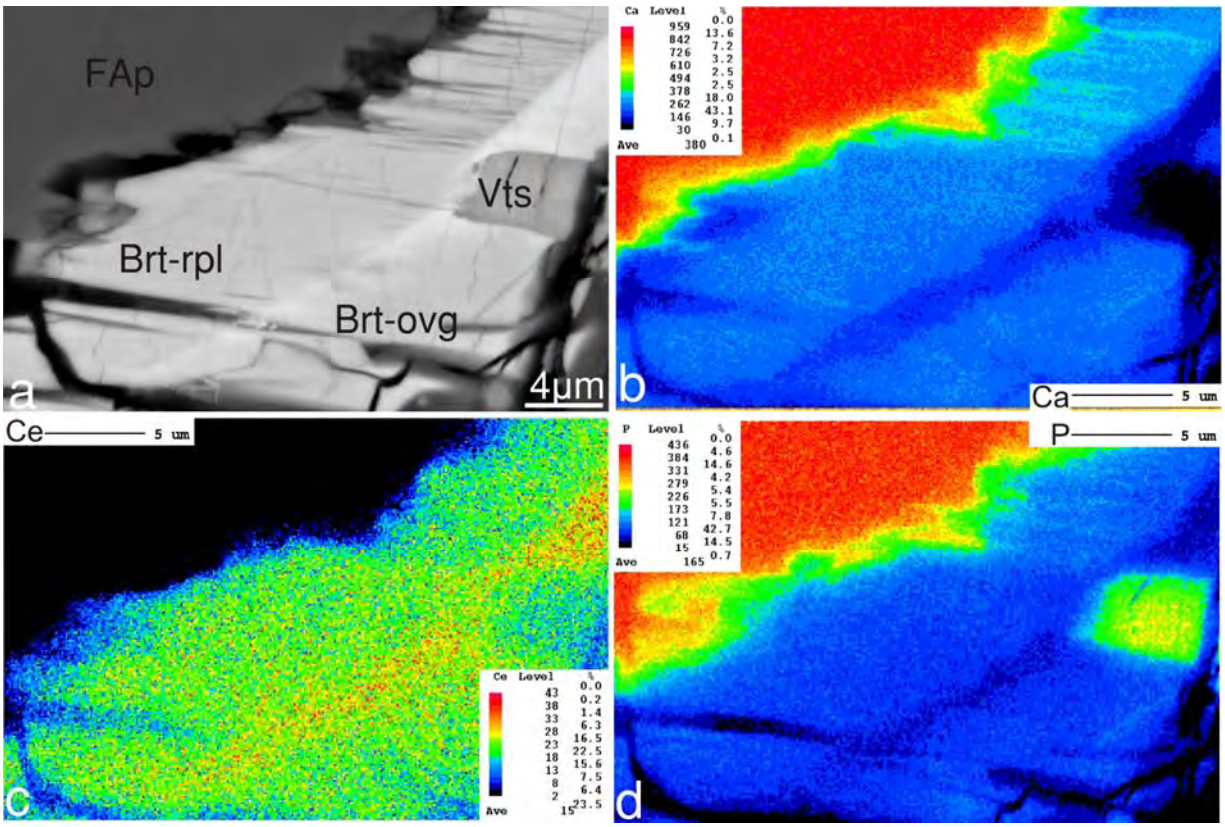

Figure 15

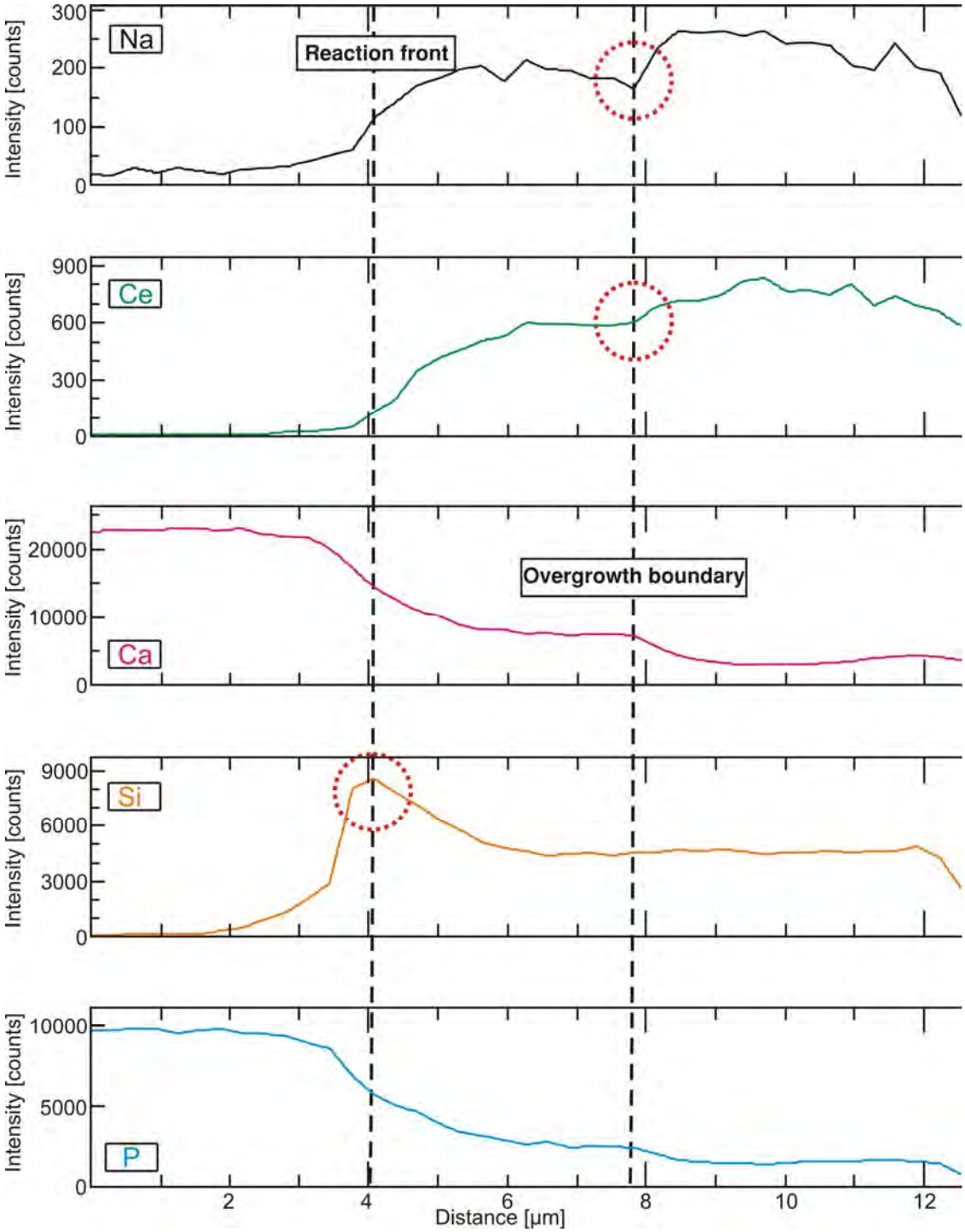
Na
Reaction front
Ce
Ca
Overgrowth boundary
Si
P
Intensity [counts]
Distance [µm]

973

Table caption: Tab.1 Experimenta

Experiment	T (°C)	P (MPa)	Time (days)	Llallagua* fluorapatite	Llallagua* monazite	Synthetic* fluorapatite	Synthetic* monazite	$Na_2Si_2O_5$*	H_2O*
LAM5	300	100	50	19.23				10.06	10.23
LAM9	300	100	50	15.5	5.42			10.28	10.3
LAM1	300	100	50			15.79	5.12	10.7	11.2
LAM6	400	100	50	19.83				9.62	9.72
LAM10	400	100	50	15.35	5.06			10.44	9.66
LAM2	400	100	50			15.23	4.8	10.08	9.91
LAM7	500	100	37	19.71				9.71	10.29
LAM11	500	100	37	15.8	5.59			11.38	9.93
LAM3	500	100	37			15.41	5.03	10.69	10.01

LAM8	600	100	13	19.51				9.97	9.86
LAM12	600	100	13	15.09	4.89			10.35	9.57
LAM9	600	100	13			15.5	5.42	10.28	10.3

*** Units of mg**

l conditions and results

Reaction producs
Fluorapatite is intact or slightly dissolved.
Fluorapatite in intact or delicately rounded. Monazite is partially replaced, dominantly by sazhinite and to a lesser extent by vitusite. Monazite reaction front is usually rugged and fragmented.
Fluorapatite is intact or delicately rounded. Monazite is partially replaced, dominantly by sazhinite and to a lesser by vitusite.
Fluorapatite is intact or very slightly dissolved. Small (few µm) dissolution pits are common.
Fluorapatite is sparingly dissolved with occasional formation of vitusite overgrowths. Formation of minute britholites around few fluorapatite faces. Monazite is replaced by vitusite or sazhinite. Monazite reaction front is usually rugged and fragmented.
Fluorapatite is sparingly dissolved with occasional formation of vitusite overgrowths. Monazite is replaced by vitusite or sazhinite.
Fluorapatite is significantly etched with formation of F-depleted zones that extend past the end of the dissolution pits
Fluorapatite is commonly overgrown by britholite with a minor replacement component. Monazite is extensively altered into vitusite. Sazhinite is no longer present. Formation of britholite corona texture around monazite. Monazite reaction front is usually rugged with some isolated fragments of unaltered monazite.
Fluorapatite is commonly overgrown by britholite with a minor replacement component. Monazite is extensively altered into vitusite. Sazhinite is no longer present. Formation of britholite corona texture around monazite.

Fluorapatite is significantly etched. Some dissolution channels cut through entire crystals. Patches of F-depleted zones are common.
Most fluorapatite crystals are partially overgrown and pseudomorphicly replaced by britholite. Monazites are altered into vitusite. Large portions of monazite is completely gone. Monazite replacement often takes a form of a symplectite.

This is a preprint, the final version is subject to change, of the American Mineralogist (MSA)
Cite as Authors (Year) Title. American Mineralogist, in press.
(DOI will not work until issue is live.) DOI: http://dx.doi.org/10.2138/am-2016-5765

Table caption: Tab.2 Selected EMP point analysy

Experiment							LAM9-10/I	LAM9-10/II	LAM7-2/I	LAM7-2/III	LAM7-2/IV
Phase description	Llallagua Fluorapatite	SD	Llallagua monazite	SD	Synthetic monazite	SD	Vts	Vts	FAp	FAp	FAp
Conditions	n= 10		n= 15		n= 10		300 °C Natural	300 °C Natural	500 °C Natural	500 °C Natural	500 °C Natural
P_2O_5	*42.40*	*0.29*	*31.07*	*0.39*	*30.61*	*0.12*	36.25	35.46	*41.30*	*41.38*	*41.48*
SiO_2	*0.00*	*0.00*	*0.01*	*0.01*	*0.02*	*0.02*	0.65	0.31	*0.00*	*0.00*	*0.00*
ThO_2	*0.00*	*0.01*	*0.01*	*0.03*	*0.00*	*0.00*	*d.l*	0.00	*0.00*	*0.00*	*0.00*
UO_2	*0.00*	*0.00*	*0.02*	*0.02*	*0.00*	*0.00*	0.00	0.07	*0.00*	*d.l*	*0.00*
Al_2O_3	*0.00*	*0.01*	*n.a*	*n.a*	*n.a*	*n.a*	0.00	*d.l*	*0.00*	*0.00*	*0.00*
Y_2O_3	*0.00*	*0.00*	*2.11*	*0.58*	*0.00*	*0.00*	0.49	0.32	*0.00*	*0.00*	*0.00*
La_2O_3	*0.02*	*0.03*	*15.78*	*1.09*	*14.73*	*0.43*	9.59	9.42	*d.l*	*d.l*	*d.l*
Ce_2O_3	*0.05*	*0.02*	*32.57*	*0.56*	*33.16*	*0.52*	18.81	18.77	*0.11*	*d.l*	*d.l*
Pr_2O3	*0.03*	*0.03*	*3.33*	*0.11*	*4.20*	*0.12*	2.50	2.06	*0.00*	*0.00*	*0.00*
Nd_2O_3	*0.03*	*0.04*	*11.37*	*0.51*	*14.00*	*0.43*	7.19	7.20	*d.l*	*0.00*	*d.l*
Sm_2O_3	*0.01*	*0.03*	*1.52*	*0.15*	*3.37*	*0.11*	0.89	0.81	*0.00*	*d.l*	*0.12*
Gd_2O_3	*0.01*	*0.02*	*1.06*	*0.15*	*0.01*	*0.02*	0.26	0.35	*0.00*	*0.17*	*0.00*
Tb_2O_3	*n.a*	*n.a*	*0.05*	*0.06*	*0.00*	*0.01*	*n.a*	*n.a*	*n.a*	*n.a*	*n.a*
Dy_2O_3	*0.02*	*0.03*	*0.52*	*0.13*	*0.04*	*0.05*	*d.l*	0.25	*d.l*	*0.00*	*0.00*
Ho_2O_3	*n.a*	*n.a*	*0.08*	*0.07*	*0.06*	*0.06*	*n.a*	*n.a*	*n.a*	*n.a*	*n.a*
Er_2O_3	*0.02*	*0.03*	*0.16*	*0.05*	*0.00*	*0.01*	0.00	d.l	*d.l*	*0.00*	*0.00*
Yb_2O_3	*0.00*	*0.00*	*0.05*	*0.03*	*0.04*	*0.03*	0.00	0.00	*d.l*	*0.00*	*0.00*
Lu_2O_3	*n.a*	*n.a*	0.04	*0.02*	0.00	*0.01*	*n.a*	*n.a*	*n.a*	*n.a*	*n.a*
CaO	54.54	*0.29*	0.25	*0.15*	0.00	*0.00*	1.93	2.05	55.83	56.15	56.46
MnO	0.28	*0.05*	*n.a*	*n.a*	*n.a*	*n.a*	*d.l*	0.00	0.25	0.28	d.l

FeO	0.01	*0.01*	*n.a*	*n.a*	*n.a*	*n.a*	0.00	0.00	0.00	0.05	d.l
SrO	0.06	*0.02*	*n.a*	*n.a*	*n.a*	*n.a*	0.00	0.00	0.05	0.06	0.00
MgO	0.00	*0.01*	*n.a*	*n.a*	*n.a*	*n.a*	0.00	0.00	0.00	0.00	0.00
PbO	*n.a*	n.a	0.01	*0.01*	0.00	*0.01*	*n.a*	*n.a*	*n.a*	*n.a*	*n.a*
Na_2O	0.01	*0.02*	*n.a*	*n.a*	*n.a*	*n.a*	22.96	24.70	0.07	0.00	0.13
F	4.37	*0.18*	*n.a*	*n.a*	*n.a*	*n.a*	0.00	0.13	3.83	3.90	2.63
Cl	0.06	*0.05*	*n.a*	*n.a*	*n.a*	*n.a*	0.04	0.04	0.00	0.02	0.01
OH	0.00		*n.a*		*n.a*		*n.a*	*n.a*	0	0	0.51
H_20	*n.a*	*n.a*	*n.a*	*n.a*	*n.a*	*n.a*	*n.a*	*n.a*	*n.a*	*n.a*	*n.a*
O=F	1.84		*n.a*		*n.a*		0.00	0.06	1.61	1.64	1.11
O=Cl	0.01		*n.a*		*n.a*		0.01	0.01	*n.a*	*n.a*	*n.a*
Total	100.10		99.99		100.23		101.55	101.87	99.93	100.46	100.38

Notes:

n	number of analyses ave
n.a	not analysed/ not applicable
d.l	below detection limit
Vts	vitusite
FAp	Fluorapatite
Brt	Britholite
SD	standard diviation

's for experimental products and starting material used in the experiments

LAM7-2/V	LAM3-5/II	LAM3-1/V	LAM3-1/VI	LAM3-1/VII	LAM3-1/VIII	LAM3-1/IX	LAM12-3/I	LAM12-3/II	LAM12-3/III	LAM12-3/IV
FAp	Brt	Brt	Brt	Brt	Brt	Brt	Vts	Brt	Brt	Brt
500 °C Natural	500 °C Synthetic	500 °C Synthetic	500 °C Synthetic	500 °C Synthetic	500 °C Synthetic	500 °C Synthetic	600 °C Natural	600 °C Natural	600 °C Natural	600 °C Natural
41.74	*9.73*	*14.05*	*13.62*	*14.68*	*14.27*	*17.62*	*34.52*	*12.79*	*11.73*	*15.09*
0.00	*24.33*	*12.02*	*12.54*	*11.63*	*12.00*	*10.07*	*3.73*	*12.78*	*13.90*	*12.49*
0.00	*synth.*	*synth.*	*synth.*	*synth.*	*synth.*	*synth.*	*0.03*	*d.l*	*d.l*	*0.02*
0.04	*synth.*	*synth.*	*synth.*	*synth.*	*synth.*	*synth.*	*d.l*	*0.00*	*0.03*	*0.00*
0.00	*synth.*	*synth.*	*synth.*	*synth.*	*synth.*	*synth.*	*0.00*	*0.00*	*0.04*	*0.04*
0.00	*synth.*	*synth.*	*synth.*	*synth.*	*synth.*	*synth.*	*0.24*	*0.58*	*0.48*	*0.60*
0.10	*11.55*	*5.76*	*6.04*	*8.02*	*8.56*	*10.49*	*10.23*	*11.01*	*13.34*	*10.60*
0.09	*25.75*	*23.02*	*24.18*	*24.79*	*27.34*	*25.19*	*18.21*	*27.19*	*28.50*	*25.06*
0.00	*3.99*	*4.03*	*3.67*	*4.16*	*3.66*	*3.95*	*1.65*	*3.55*	*2.97*	*2.63*
0.00	*12.42*	*16.41*	*16.33*	*15.50*	*14.67*	*12.85*	*5.80*	*11.55*	*10.92*	*9.50*
0.00	*2.72*	*10.40*	*10.53*	*5.98*	*5.87*	*3.82*	*0.79*	*1.37*	*1.43*	*1.46*
0.00	*synth.*	*synth.*	*synth.*	*synth.*	*synth.*	*synth.*	*0.28*	*0.85*	*0.83*	*0.69*
n.a	*n.a*	*n.a*	*n.a*	*n.a*	*n.a*	*n.a*	*n.a*	*n.a*	*n.a*	*n.a*
0.15	*synth.*	*synth.*	*synth.*	*synth.*	*synth.*	*synth.*	*0.00*	*0.54*	*0.36*	*0.29*
n.a	*n.a*	*n.a*	*n.a*	*n.a*	*n.a*	*n.a*	*n.a*	*n.a*	*n.a*	*n.a*
0.00	*synth.*	*synth.*	*synth.*	*synth.*	*synth.*	*synth.*	*0.00*	*0.22*	*d.l*	*0.00*
0.00	*synth.*	*synth.*	*synth.*	*synth.*	*synth.*	*synth.*	*0.00*	*0.00*	*0.00*	*0.11*
n.a	*n.a*	*n.a*	*n.a*	*n.a*	*n.a*	*n.a*	*n.a*	*n.a*	*n.a*	*n.a*
55.59	4.58	8.03	8.89	8.43	8.37	11.67	5.48	13.50	11.40	16.39
0.27	*synth.*	*synth.*	*synth.*	*synth.*	*synth.*	*synth.*	0.00	0.00	0.06	0.00

0.06	*synth.*	*synth.*	*synth.*	*synth.*	*synth.*	*synth.*	0.00	0.00	0.00	0.00
0.03	*synth.*	*synth.*	*synth.*	*synth.*	*synth.*	*synth.*	0.00	0.00	0.00	0.00
0.00	*synth.*	*synth.*	*synth.*	*synth.*	*synth.*	*synth.*	0.05	0.00	0.00	0.00
n.a	*n.a*	*n.a*	*n.a*	*n.a*	*n.a*	*n.a*	*n.a*	*n.a*	*n.a*	*n.a*
0.03	5.38	5.14	5.03	5.59	4.90	5.20	21.95	3.01	3.67	2.85
4.10	1.76	1.68	1.74	1.85	1.77	1.96	0.00	1.09	1.24	1.23
0.01	*synth.*	*synth.*	*synth.*	*synth.*	*synth.*	*synth.*	0.02	0.08	0.06	0.04
0	0.52	0.43	0.42	0.36	0.40	0.38	n.a	0.695	0.635	0.695
n.a	*n.a*	*n.a*	*n.a*	*n.a*	*n.a*	*n.a*	*n.a*	*n.a*	*n.a*	*n.a*
1.73	0.74	0.71	0.73	0.78	0.75	0.82	0.00	0.46	0.52	0.52
n.a	*n.a*	*n.a*	*n.a*	*n.a*	*n.a*	*n.a*	0.00	0.02	0.01	0.01
100.47	101.99	100.26	102.26	100.21	101.06	102.37	102.98	100.33	101.07	99.24

LAM12-3/V
Vts
600 °C Natural
39.05
3.06
0.00
0.00
0.02
0.32
10.01
17.91
1.75
6.04
0.79
0.42
n.a
d.l
n.a
0.00
0.00
n.a
8.17
0.00

0.00
0.00
d.l
n.a
10.78
0.00
0.02
n.a
n.a
0.00
0.00
98.34